Doctoral Thesis:
Unconventional properties of the antiperovskite oxide superconductor $Sr_{3-x}SnO$ and a related compound

Department of Physics, Kyoto University
Atsutoshi IKEDA

Supervisor: Prof. Yoshiteru MAENO

February 2, 2020

Abstract

This thesis reports unconventional properties of $Sr_{3-x}SnO$ in the normal [1, 2] and superconducting [3] states and discovery of superconductivity in a related compound $CaSb_2$ [4].

Sr_3SnO belongs to antiperovskite oxides and is theoretically predicted to be a Dirac semimetal or a topological crystalline insulator [5, 6]. Assuming the naive ionic states of Sr^{2+} and O^{2-}, unusual metallic anion Sn^{4-} is expected to satisfy the charge neutrality as $\left(Sr^{2+}\right)_3Sn^{4-}O^{2-}$. However, Sn^{4-} state is unstable and a small part of the electrons (let us express as 3ϵ) moves to Sr, forming the virtual ionic state of $\left[Sr^{(2-\epsilon)+}\right]_3Sn^{(4-3\epsilon)-}O^{2-}$. In the band structure, there is an energy inversion between the filled Sn-5p and unoccupied Sr-4d bands at the Γ point in the Brillouin zone. This band inversion makes Sr_3SnO a topological crystalline insulator with a massive Dirac cone.

We found superconductivity with Sr-deficient (hole-doped) $Sr_{3-x}SnO$ in 2016 [7]. Reflecting the topological nature in the normal state, topological superconductivity is possible if Cooper pairs make use of the band mixing [7,8]. Since a large amount of deficiency $x \simeq 0.5$ is needed for superconductivity, first we investigated whether there is any structural change due to deficiency [1]. By x-ray diffraction using a synchrotron, we did not find a sign of structural deformation. Then we calculated the band structure of $Sr_{2.5}SnO$ to see where the Fermi energy is located. We found that the Fermi energy is lowered by 0.8 eV, which is about 10-times larger than the band-inverted region. Thus, a smaller amount of Sr deficiency would be favorable for topological superconductivity.

We also looked back at the original motivation for antiperovskite oxides, namely the Sn^{4-} state. We had observed Sn^{4-} by Mössbauer spectroscopy at room temperature, but at the same time, we had also detected another ionic state of Sn [9]. The origin of the additional state was not fully understood. Therefore, we performed temperature-dependent Mössbauer spectroscopy and compared the results with the first-principles calculations [2]. As a result, we revealed that the Sn atoms in the additional state are neighboring the vacancies of Sr, while the other Sn atoms keep their ionic state of Sn^{4-}.

Next, we carried out muon spin spectroscopy of $Sr_{3-x}SnO$ to investigate its superconducting state [3]. We observed a clear superconducting transition and confirmed the bulk superconductivity. The evaluated penetration depth λ is long for the transition temperature T_c, and the ratio T_c/λ^{-2} was found to be comparable to those of unconventional superconductors. Under zero magnetic field, we did not detect the sign of broken time-reversal symmetry. These features can be explained both by the theoretically predicted topological superconductivity and by the ordinary s-wave one.

While investigating properties of $Sr_{3-x}SnO$, we searched for a new antiper-

ovskite oxide superconductor. While we synthesize many samples with various combinations and compositions of the constituent elements, we found that one of the side products, $CaSb_2$, is a new superconductor [4]. $CaSb_2$ crystallizes in a non-symmorphic structure. Interestingly, the bulk electronic band structure of $CaSb_2$ has multiple nodal lines in the Brillouin zone protected by the mirror and non-symmorphic screw symmetries [10]. These nodal lines are stable even in the presence of the spin-orbit interaction, in contrast to many others that are not protected by the non-symmorphic symmetries.

History of the modern researches on topology in condensed matter began with the topological insulators, whose band structure has no nodes. Then, Dirac and Weyl semimetals, with nodal points, were interpreted as topological. Today, materials with nodal lines are one of the hot topics in condensed-matter physics. Beside the researches on the normal state, there have been researches on the superconductivity induced in such topological materials. Indeed, a doped topological insulator $Cu_xBi_2Se_3$ was experimentally found to be a topological superconductor, and a doped Dirac semimetal $Sr_{3-x}SnO$ is also a candidate of a topological superconductor. The next step should be the nodal-line superconductors. In this sense, superconductivity in $CaSb_2$, a material with the Dirac nodal lines, will be interesting.

We hope that our study on Dirac-point superconductor $Sr_{3-x}SnO$ and Dirac-line superconductor $CaSb_2$ will trigger further studies on topological phenomena including topological superconductivity in topological nodal materials.

Contents

Chapter 1 Introduction 7
1.1 Topological materials 7
1.2 Motivation 9
1.3 Overview of this thesis 10

Chapter 2 Review of literature 11
2.1 Antiperovskite oxides 11
2.2 $CaSb_2$ 24

Chapter 3 Experiment 27
3.1 Sample syntheses 27
3.2 X-ray diffraction 28
3.3 Magnetic susceptibility 29
3.4 Electrical transport 29
3.5 Heat capacity 29
3.6 Mössbauer spectroscopy 30
3.7 Muon spin spectroscopy 32
3.8 First-Principles Calculation 33

Chapter 4 Band structure calculation of $Sr_{3-x}SnO$ 37
4.1 High-energy XRD 37
4.2 Band-structure calculations 38

Chapter 5 Hole-doped anionic states of Sn in $Sr_{3-x}SnO$ revealed by Mössbauer spectroscopy 43
5.1 Sample characterization 43
5.2 Mössbauer spectra 45
5.3 First-principles calculations 50
5.4 Comparison with NMR 52
5.5 Conclusion of this chapter 54

Chapter 6 Possible unconventional superconductivity in $Sr_{3-x}SnO$ investi-

gated by μSR 55
6.1 Magnetic susceptibility and specific heat 55
6.2 μSR under 30 mT 57
6.3 μSR under 5 and 0 mT 63
6.4 Conclusion of this chapter 64

Chapter 7 Discovery of superconductivity in $CaSb_2$ 67
7.1 Evidence of superconductivity 67
7.2 Discussion 72
7.3 Conclusion of this chapter 73

Chapter 8 Conclusion 75
8.1 Summary 75
8.2 Future perspective 76

Bibliography 79

Chapter 1

Introduction

1.1 Topological materials

Topology in condensed matter have been extensively studied in recent years [11–13]. Topology is originally a mathematical concept that classifies the shapes of abstract things by discrete numbers. In condensed-matter physics, materials are classified by the shape of the electronic band structure. For example, the number of energy inversions of the bands with different parities in the Brillouin zone serves as a topological number for insulators in the presence of the time- and spatial-inversion symmetries.

One of the important consequences of topological classification is that there has to be a surface state on the boundary between two materials with different topological numbers. In the case of topological insulators, there is a metallic state on the surface, or boundary with vacuum, even though inside is insulating, as shown in Fig. 1.1. Since the topological number is discrete, it cannot change continuously on the boundary. In order to change the topological number, there has to be a region in which the topological number is undefined (or ill-defined). That surface state is protected by topology, and therefore stable against perturbations as long as the perturbation does not change the symmetry of the system. The surface state of topological materials are studied for application to energy-efficient devices and spintronics.

Moreover, topological classification also applies to superconductors [14–16]. Some candidates for topological superconductors are listed in Table 1.1. Some topological superconductors have a peculiar quasiparticle called Majorana fermion as a surface state, which can be used for quantum computing. Topological superconductivity can be induced to topological insulators, and indeed topological superconductivity was found in a carrier-doped topological insulator $Cu_xBi_2Se_3$ [17–20].

These days, Dirac and Weyl semimetals are regarded as new kinds of topological

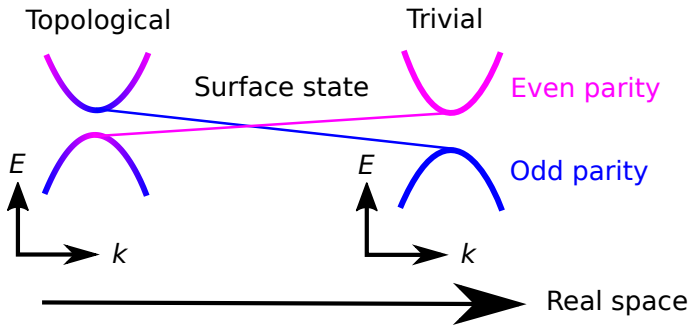

Fig. 1.1 Schematic image of the surface state between the trivial and topological insulators. Each parabola is the conduction or valence band in the reciprocal space. The surface state is localized in the real space on the boundary of the topological and trivial insulators.

Table 1.1 List of candidates for topological superfluids and superconductors.

Normal State	Superconducting State	Material
Trivial (Fermi liquid)	Topological, Full gap	^{3}He-B phase [21]
Trivial (Fermi liquid)	Topological, Point node	^{3}He-A phase [21]
Trivial (Fermi liquid)	Topological?	Sr_2RuO_4 [22]
Trivial (Fermi liquid)	Topological?	U based (UBe_{13} [23], etc.)
Topological insulator (Full gap)	Topological, Full gap?	$Cu_xBi_2Ce_3$ [20]
Dirac semimetal (Point node)	Topological?	Cd_3As_2 [24]
Dirac semimetal (Point node)	**Unknown**	**$Sr_{3-x}SnO$** [7]
Dirac-line material (Line node)	Unknown	$BaNbS_3$ [25]
Dirac-line material (Line node)	**Unknown**	**$CaSb_2$** [4]
⋮	⋮	⋮

materials [26, 27]. Usually, the crossing point of the electronic bands opens a gap due to hybridization of the bands. However, in the presence of certain symmetries, the hybridization is prohibited or suppressed and as a result the crossing point remains as a Dirac or Weyl point. The materials with these band crossing point at the Fermi energy are called Dirac or Weyl semimetals. Such gapless points exhibit peculiar properties such as ultrahigh mobility, chiral anomaly, and surface Fermi arcs. We can also consider inducing topological superconductivity to Dirac and Weyl semimetals [8, 28, 29]. Superconductivity is experimentally found in a pressurised Dirac semimetal Cd_3As_2 [30] and a doped Dirac semimetal $Sr_{3-x}SnO$ [7]. These compounds are the leading candidates of topological superconductors.

More recently, the concept of the Dirac and Weyl semimetals has been extended to the line-nodal materials. In contrast to the gapless point in the Dirac and Weyl semimetals, the band crossing in the line-nodal materials forms a line in the

Brillouin zone [31–33]. Several notable phenomena beyond the point-nodal properties, such as a long-ranged Coulomb interaction [34], a large surface polarization charge [35], and quasitopological electromagnetic response [36], are theoretically predicted. Furthermore, if superconductivity is induced in the materials with a Fermi surface surrounding the nodal line, topological crystalline and second-order topological superconductivity is possible [37].

1.2 Motivation

We reported the first superconductivity among antiperovskite oxides in Sr-deficient $Sr_{3-x}SnO$. We consider this class of oxides is interesting for the following two reasons.

One motivation is somewhat chemical: negative ionic state of metallic elements. Metallic elements tend to be cations and thus metallic anions are rare especially in oxides, in which oxygen becomes anion and others become cations to satisfy the charge neutrality. We do not have much knowledge of what happens if the p orbitals of Sn or Pb are filled in oxides. In order to investigate the ionic state of Sn, Mössbauer spectroscopy serves as a powerful tool. Because Mössbauer spectroscopy has a resolution of as high as 10^{-12}, we can observe a slight change in the ionic state due to Sr deficiency.

The other motivation is the physical aspect: topological nature. This is actually related to the first motivation. Because the p orbitals of Sn or Pb is occupied, we can make use of the d orbitals of alkaline-earth elements as conduction bands, Otherwise the d orbitals will be located far above the Fermi energy. Although topology has been one of the hottest topics in recent condensed-matter physics, experimental realization of the topological insulators or superconductors is still limited. We performed muon spin rotation/relaxation (μSR) experiments in order to evaluate a fundamental parameter of superconductivity, namely, the London penetration depth. μSR is also sensitive to breaking of time-reversal symmetry.

While investigating $Sr_{3-x}SnO$, we kept searching for a new superconductor. Discovery of superconductivity has a great impact. For example, high-temperature cuprate superconductors [38] have been playing a central role in condensed matter physics and deepened our understanding of the strongly correlated electron system. Superconductivity in H_3S [39] opened a new class of superconductors, hydride superconductors, and the highest record of superconducting transition temperature now reaches 260 K in LaH_{10} [40]. These success stories motivated us to look for a new superconductor.

1.3 Overview of this thesis

In the next chapter, we review previous works on antiperovskite oxides. We begin with the initial theoretical prediction of the bulk Dirac cone and move to experimental studies motivated by theory in Chapter 2. In the latter part of Chapter 2, we focus on the superconductivity in $Sr_{3-x}SnO$. Chapter 3 is dedicated to explain the experimental setup. Results of our band-structure calculations on $Sr_{3-x}SnO$, published in Ref. [1], is presented in Chapter 4.1. In Chapter 5, we write about the identification of the γ-ray absorption in the Mössbauer spectra based on Ref. [2]. μSR study on the superconducting state is shown in Chapter 6. Chapter 7 describes discovery of superconductivity in $CaSb_2$. Finally we summarize this thesis in Chapter 8.

Chapter 2

Review of literature

2.1 Antiperovskite oxides

2.1.1 Theoretical aspect

Antiperovskite (also called inverse perovskite) oxides A_3BO (A: alkaline-earth elements, Eu, or Yb; B: group-14 elements) are the metal-rich counterpart of the ordinary perovskite oxides ABO_3 . Figure 2.1 compares the crystallines structures of the ordinary and anti-perovskite oxides. Both of them have the same structure with a space group $Pm\bar{3}m$ (No. 221, O_h^1) [41]. In ordinary perovskite oxides, metallic element is octahedrally coordinated by oxygen. In contrast in antiperovskite oxides, oxygen is surrounded by metallic element. Thus, the positions of the metallic and non-metallic elements are inverted.

As a consequence of three A^{2+} ions in a unit cell, the ionic state of B is forced to be $4-$ to satisfy the charge neutrality condition as $\left(A^{2+}\right)_3 B^{4-}\mathrm{O}^{2-}$. Compared

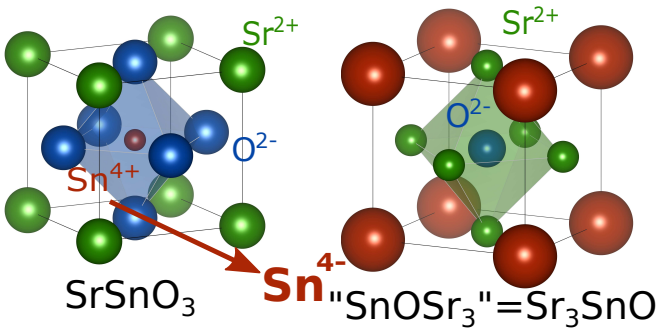

Fig. 2.1 Comparison of the crystalline structures of the ordinary perovskite oxide $SrSnO_3$ and antiperovskite oxide Sr_3SnO. This figure is reprinted from Ref. [7].

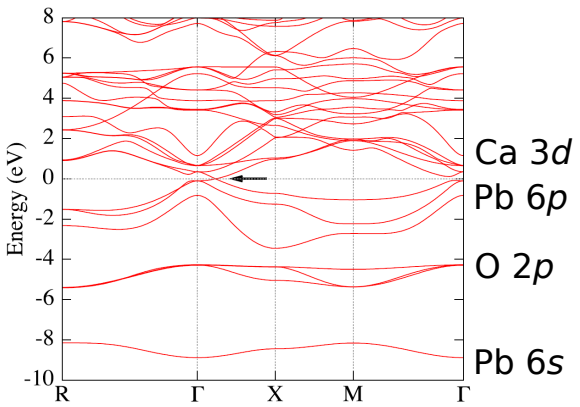

Fig. 2.2 Result of a first-first principles calculation on Ca_3PbO. The filled Pb $6p$ bands support the unusual metallic anion Pb^{4-}. The arrow indicates the Dirac cone. This figure is reprinted from Ref. [5].

to B^{4+} in ordinary perovskite oxides, a charge-inverted ion is in antiperovskite oxides. The unusual metallic anion such as Sn^{4-} and Pb^{4-} is also supported by the first-principles calculations [5, 6]. Indeed, the calculations suggest that the valence band of A_3BO originates from the filled p orbitals of B, meaning the ionic state of B^{4-} (Fig. 2.2). This metallic anion such as Sn^{4-} and Pb^{4-} is rare especially in oxides.

Band-structure calculations further revealed that some antiperovskite oxides with heavy constituent elements have an energy inversion between the valence B-p and conduction A-d bands at the Γ point in the Brillouin zone [5]. Figure 2.3 shows the calculated band structures of various antiperovskite oxides. We can see that the band gap closes and eventually two bands are energetically inverted. Since the p electrons of B^{4-} have a very high energy, a part of the electrons is pushed out to A^{2+} to form an ionic state of $\left[A^{(2-\epsilon)+}\right]_3 B^{(4-3\epsilon)-}O^{2-}$. Usually, band inversion leads to hybridization and gap opening at the crossing point. However, in the case of antiperovskite oxides, hybridization of the bands is prohibited by the symmetries of the crystal and orbitals on the high-symmetry line in the Brillouin zone, as depicted in Fig. 2.4. Therefore, the crossing point remains gapless as a three-dimensional Dirac cone at the Fermi energy.

In the presence of the spin-orbit coupling, hybridization is allowed by perturbation and there opens a gap of the order of 10 meV at the Dirac point [42]. With this small gap, antiperovskite oxides with band inversions turn into topological crystalline insulators [6]. Due to the crystalline symmetry, the valence and conduction bands are four-fold degenerate at the Γ point. Hence, two band inversions take place simultaneously at the Γ point. Then, the Z_2 invariant, calculated

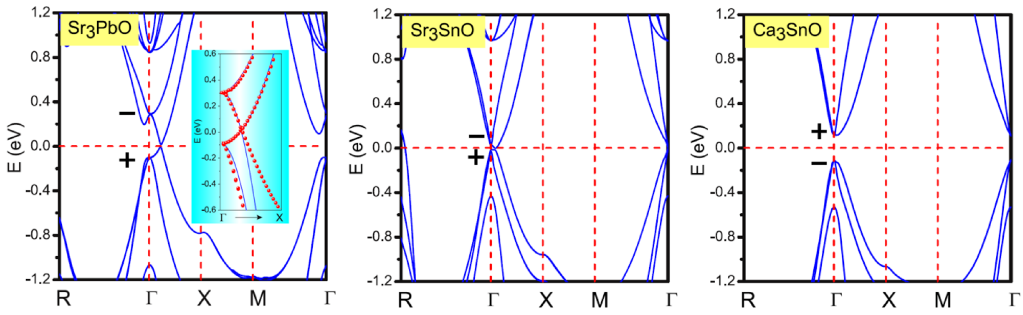

Fig. 2.3 Band-structure calculations on Sr_3PbO, Sr_3SnO, and Ca_3SnO. While Ca_3SnO is a trivial insulator, Sr_3PbO is a topological crystalline insulator with a band inversion and a resultant Dirac cone. Sr_3SnO is on the vicinity of the topological transition with a barely inverted bands. This figure is reprinted from Ref. [6].

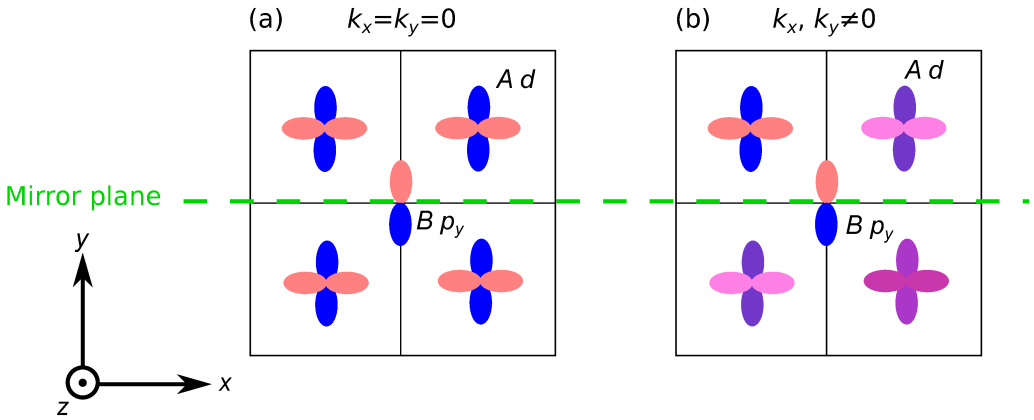

Fig. 2.4 Schematic images of the band hybridization (a) on and (b) away from the k_z axis. On the high-symmetry line in the Brillouin zone, the valence B-p and conduction A-d bands belong to different symmetry with respect to the mirror operation. Therefore, hybridization between these bands is forbidden and the band-crossing point remains as a Dirac cone. On the other hand, if the wave vector is off the high-symmetry line, the two bands can mix due to the phase rotation of the wavefunctions.

from the number of the band inversion, is trivial even in the band-inverted antiperovskite oxides. However, in terms of another topological invariant called the mirror Chern number, antiperovskite oxides are topological. The mirror Chern number is defined as the difference in the Chern number of bands belonging to different mirror subsectors. Since the four bands degenerate at the Γ point are divided into different mirror subsectors, the mirror Chern number becomes non-zero

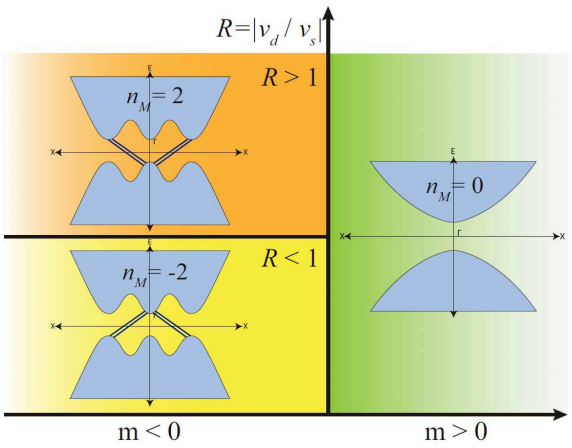

Fig. 2.5 Topological phase diagram of antiperovskite oxides for the (100) mirror plane. As the band gap m becomes positive (no band inversion) to negative (band inversion), the mirror Chern number changes by 2. In the band inverted regime, there are two topological phases depending on the band parameter v_d and v_s. Each inset is a schematic band structure of the bulk (light blue) and surface (dark blue) states. The two topological phases have the opposite sign of the mirror Chern number and correspondingly surface states with the opposite directions. This figure is reprinted from Ref. [6].

in the band-inverted antiperovskite oxides, as summarized in Fig. 2.5.

Interestingly, the band structure or topology of this class of oxides can be tuned by chemical substitution [43]. As we substitute A from Ca to Ba, we can lower the energy of the conduction band or increase the size of the band inversion. In addition, the size of the gap in the Dirac cone is small with B = Sn and large with B = Pb (Fig. 2.6). We have rich variety of materials such as a trivial insulator Ca_3SnO, topological crystalline insulator with a Dirac cone Sr_3PbO, and a metal with two Dirac cones Ba_3SnO. This tunability makes antiperovskite oxides a good platform to study the topological and Dirac nature.

2.1.2 Experimental works

After the initial theoretical predictions, many experimentalists have been working on antiperovskite oxides. First, the crystalline structure of various antiperovskite oxides were extensively studied using the x-ray diffraction using single crystals [44]. As a result, it was found that some antiperovskite oxides such as $Ba_3(Sn, Pb)O$ undergo a structural transition to orthorhombic at low temperature. The transition temperatures of the various antiperovskite oxides are summarized in Fig. 2.7. We comment that Sr_3SnO, the topic of this thesis, is expected to keep the cubic

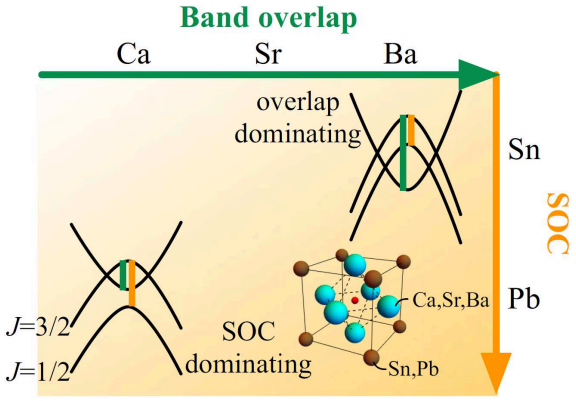

Fig. 2.6 Evolution of the band structure with chemical substitution. Ca_3SnO does not have band inversion nor Dirac cone, while Ba_3SnO possesses two Dirac cones. This figure is reprinted from Ref. [43].

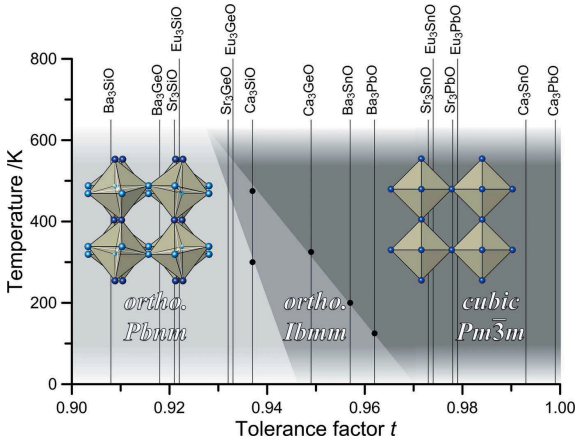

Fig. 2.7 Structural phase diagram of various antiperovskite oxides. While Ba_3SnO undergo a transition to orthorhombic at low temperature, Sr_3SnO remains cubic down to 0 K. This figure is reprinted from Ref. [44].

structure down to 0 K.

Many other studies are focused on giving the experimental evidence of the unusual band structure. The three-dimensional Dirac cone was for the first time observed in Ca_3PbO by angle-resolved photoemission spectroscopy (ARPES) [45]. The authors found that their Ca_3PbO sample is hole doped due to spontaneous Ca deficiency, and then they succeeded in partial compensation of the carriers by substitution of Pb with Bi. They later performed magnetoresistance and tunnel-diode-oscillation measurements and obtained results consistent with the bulk Dirac cone [46]. Another evidence for the Dirac nature was given by the magnetotrans-

port on Sr_3PbO, revealing a cyclotron mass as small as 1% of the free electron mass [47].

Okamoto *et al.*, investigated the thermoelectric properties of $Ca_3(Sn, Pb)O$. For high thermoelectric performance, multivalley band structure is effective. Antiperovskite oxides crystallize in a cubic structure, and thus there are six equivalent Dirac cones along the Γ-X line in the Brillouin zone. Due to these multiple Fermi surfaces, high thermoelectric power is expected. The authors observed a much larger thermoelectric power in Ca_3SnO than in Ca_3PbO because of the coexistence of moderately high mobility and large effective mass.

2.1.3 Superconductivity in $Sr_{3-x}SnO$

In this section, we review the superconductivity in $Sr_{3-x}SnO$, mainly based on our previous studies.

In 2016, we discovered superconductivity in Sr-deficient $Sr_{3-x}SnO$ ($x \simeq 0.5$) [7]. This was the first superconductivity among antiperovskite oxides. As shown in Fig. 2.8, superconductivity was evidenced by zero resistivity and Meissner effect. The resistivity starts to drop at $T_c = 4.9$ K and reaches zero at 4.5 K. Meissner effect was observed in the alternating- and direct-current (AC and DC) magnetic susceptibility with an onset of about 4.5 K, as well as the peak in the imaginary part of the AC susceptibility. Figure 2.9 presents the superconducting phase diagram deduced from the field dependence of resistivity. T_c at each field was defined as the point where the resistivity becomes 50% or 10% of the normal-state value. Using the Werthamer-Helfand-Hohenberg (WHH) relation [48], the upper critical field at 0 K was estimated to be $\mu_0 H_{c2} = 0.44$ T, adopting the 10% criterion for T_c. Here, μ_0 denotes the magnetic permeability of vacuum. The Ginzburg-Landau (GL) coherence length was then estimated to be $\xi_{GL} = \sqrt{\Phi_0/(2\pi\mu_0 H_{c2})} = 27$ nm, where Φ_0 is the magnetic flux quantum.

Figure 2.10 shows the AC susceptibility down to 0.15 K of a sample different from the one in Fig. 2.9. In addition to the superconducting transition at around 5 K, there is another transition at 0.8 K. This second transition (hereafter referred to as 0.8-K phase) is reproducible in all the superconductive samples measured down to 0.15 K. Thus, we consider that the 0.8-K phase originates from another superconducting phase with a different value of deficiency x.

Reflecting the topological nature in the normal state, $Sr_{3-x}SnO$ has a possibility of exhibiting a topological crystalline superconductivity. Figure 2.11 presents the band structure and Fermi surface of the hole-doped Sr_3SnO assuming the rigid band shift. As we can see in Fig. 2.11(b), there is a strong orbital mixing due to the energy inversion between the valence and conduction band. Along the Γ-X line (k_x, k_y, or k_z axes), orbital mixing is suppressed by crystalline symmetry and the p orbital is dominant. If the Cooper pairs are formed by the electrons

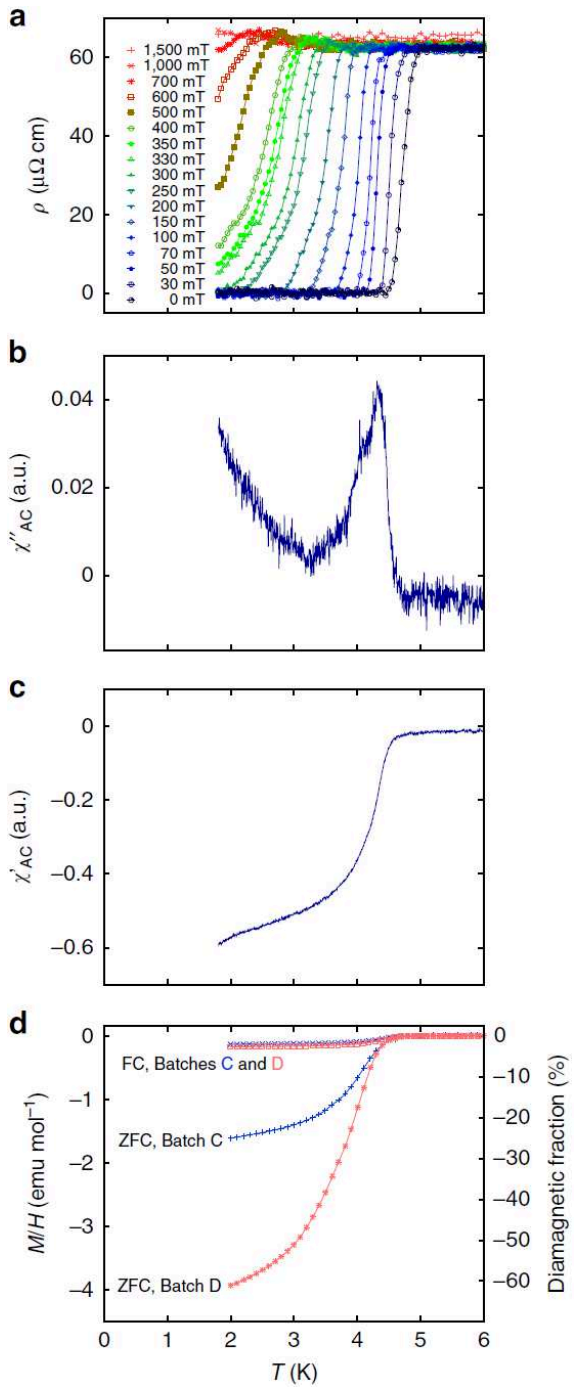

Fig. 2.8 (a) Electrical transport, (b) imaginary and (c) real parts of the AC susceptibility, and (d) the DC susceptibility of $Sr_{3-x}SnO$. This figure is reprinted from Ref. [7].

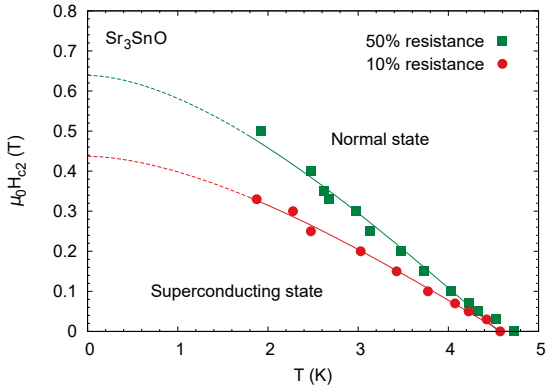

Fig. 2.9 Superconducting phase diagram of $Sr_{3-x}SnO$. The curves present the results of fitting with the Werthamer-Helfand-Hohenberg relation. This figure is reprinted from Ref. [7].

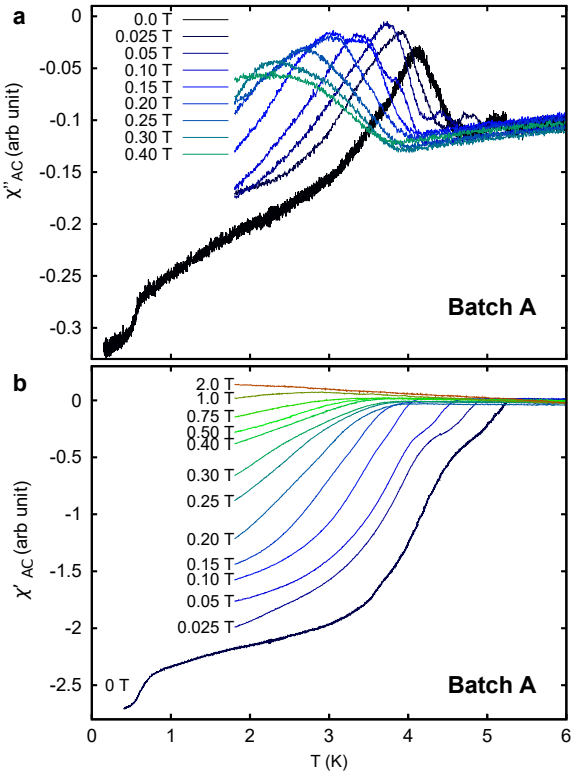

Fig. 2.10 (a) Imaginary and (b) real parts of the AC susceptibility of a different batch. This figure is reprinted from Ref. [7].

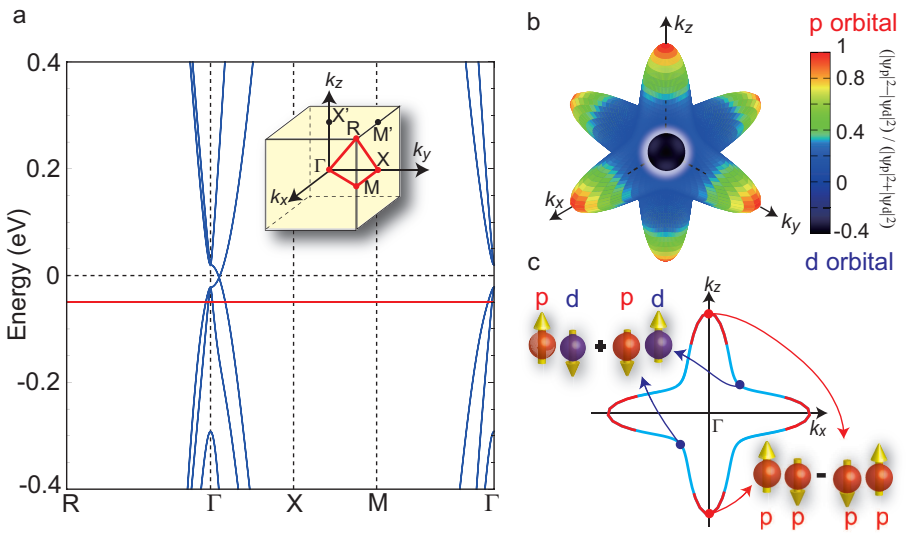

Fig. 2.11 (a) Band structure of Sr_3SnO. The red line indicates the slightly hole doped Fermi energy. The inset is the Brillouin zone of the simple cubic lattice. (b) Fermi surface when the Fermi energy is located at the position pointed by the red line in the panel (a). The color indicates the contribution from the Sn-p and Sr-d orbitals. Along the high-symmetry line k_x, k_y, k_z, p orbital is dominant because of the suppression of the band hybridization, indicated by the red color. Away from the k_x, k_y, k_z axes, p and d orbitals are strongly mixed, indicated by the blue color. (c) Possible symmetries of Cooper pairs. This figure is reprinted from Ref. [7].

from the same orbitals, as indicated by the red arrows in Fig. 2.11(c), even-parity spin-singlet pairing is realized. However, if the Cooper pairs make use of the band mixing and form a inter-orbital pairs, as indicated by the blue arrows in Fig. 2.11(c), odd-parity spin-triplet pairing is favored.

Kawakami *et al.* developed a theory of the topological crystalline materials with the total angular momentum $j = 3/2$ and deduced a topological superconductivity with a high winding number [8]. They calculated the transition temperatures of various superconducting symmetries, and found that A_{1u} state, the same symmetry as the Balian-Werthamer (BW) state, has the highest T_c as shown in Fig. 2.12(a). We also note that as we increase the hole doping μ, the A_{1g} state becomes more stable. The gap structure of the A_{1u} state is shown in Fig. 2.13. The A_{1u} state is fully gapped, but due to the suppression of the band hybridization along the Γ-X line, the gap amplitude is also suppressed.

It is noticeable that the T_{1u} symmetry has a transition temperature comparable to that of the A_{1u} state. The gap structure is shown in Fig. 2.14. T_{1u} symmetry has point nodes along the k_z axis, but not in the k_x or k_y axis. Therefore, it is a

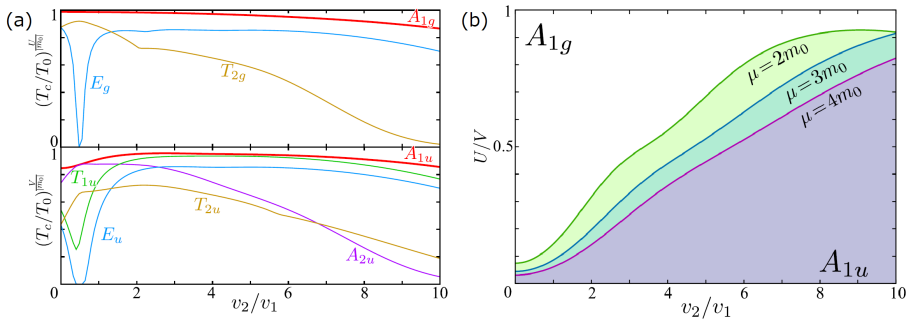

Fig. 2.12 (a) Transition temperatures of superconducting states with various symmetries. $v2/v1$ determines the shape of the band structure. In $Sr_{3-x}SnO$, $v2/v1$ is close to 3. U and V are the intra- and inter-orbital interactions, respectively. Among the even- and odd-parity superconductivity, A_{1g} (ordinary s wave) and A_{1g} (same symmetry as the BW state) have the highest T_c, respectively. (b) Comparison of the transition temperatures of the A_{1g} and A_{1u} states. A_{1u} is realized if V is much larger than U. As we increase the hole-doping level μ, A_{1g} becomes more stable. m_0 denotes the amount of band inversion. This figure is reprinted from Ref. [8].

nematic superconductivity breaking the rotational symmetry of the crystal. The difference between the A_{1u} and T_{1u} states will be detected via the presence of the point nodes or the breaking of the rotational symmetry.

In our initial samples, synthesized under vacuum (Method A in Table 2.1), the amount of the Sr deficiency was not clear because the deficiency was loaded via uncontrolled evaporation of Sr during the synthesis. Then, we improved the synthesis procedures by introducing some amount of Ar gas (Method B in Table 2.1) so that we can suppress the Sr evaporation and control the amount of Sr deficiency by initial loading [49]. Table 2.1 summarizes the methods we tried and superconducting volume fractions of the products. We comment that even with the improved Method B, the actual amount of deficiency x in $Sr_{3-x}SnO$ is not fully controlled; the Sr deficiency by initial composition is still nominal. Hereafter we use x for the actual amount and x_0 for the nominal amount of Sr deficiency.

The actual amount of Sr deficiency x was measured by energy-dispersive x-ray spectroscopy (EDX). The results of EDX for three samples are shown in Fig. 2.15. Although the distribution of Sr/Sn ratio is centered at Sr/Sn = 2.5 or $x = 0.5$, the sample has large spatial distribution of x. This distribution probably causes the separation into the superconductive and non-superconductive phases discussed below.

We synthesized a number of samples with various nominal deficiency x_0 and investigated the evolution of superconductivity. As shown in Fig. 2.16(a), the

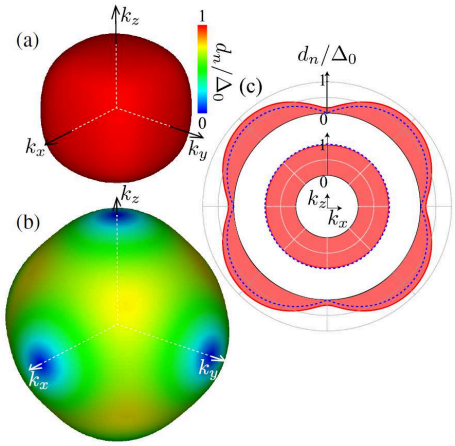

Fig. 2.13 Gap structure of the A_{1u} superconducting state on the (a) inner and (b) outer Fermi surfaces. (c) Cross sectional view of the gap structure. This figure is reprinted from Ref. [8].

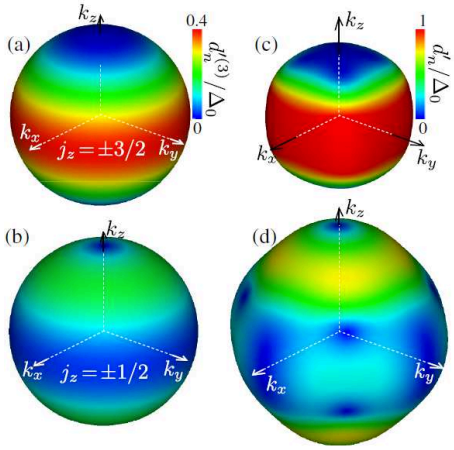

Fig. 2.14 Gap structure of the T_{1u} state on the (a, c) outer and (b, d) inner Fermi surfaces. The panels (a) and (b) are calculated with the band parameter $v_2 = 0$. (c) and(d) are calculated with $v_2 = 3v_1$, as in antiperovskite oxides. This figure is reprinted from Ref. [8].

Table 2.1 Summary of the synthesis methods and the superconducting volume fraction estimated from temperature T dependence of DC magnetization $M(T)$ [49]. Method B resulted in particularly good superconductive samples. Since the actual amounts of deficiency x in Samples B-2 and B-3 were not fully controlled, we express the composition of the products with quotation marks.

Sample name	Product	Starting composition	Atmosphere at RT	Reaction T	Strontium purity	$\frac{M}{M_{\text{Meissner}}}$	Estimated volume fraction
A-1	Sr_3SnO	3.75Sr+SnO	Vacuum	800°C	99.9%	< 0.015	< 1.0
A-2	$Sr_{3-x}SnO$	3.0Sr+SnO	Vacuum	800°C	99.9%	0.23	15
B-1	Sr_3SnO	3.0Sr+SnO	30 kPa Ar	825°C	99.9%	0	0
B-2	"$Sr_{2.5}SnO$"	2.5Sr+SnO	30 kPa Ar	825°C	99.9%	0.64	43
B-3	"$Sr_{2.5}SnO$"	2.5Sr+SnO	30 kPa Ar	825°C	99.99%	1.05	70
C-1	Sr_3SnO	3.1Sr+SnO	23 kPa Ar	1200°C	99.99%	0	0

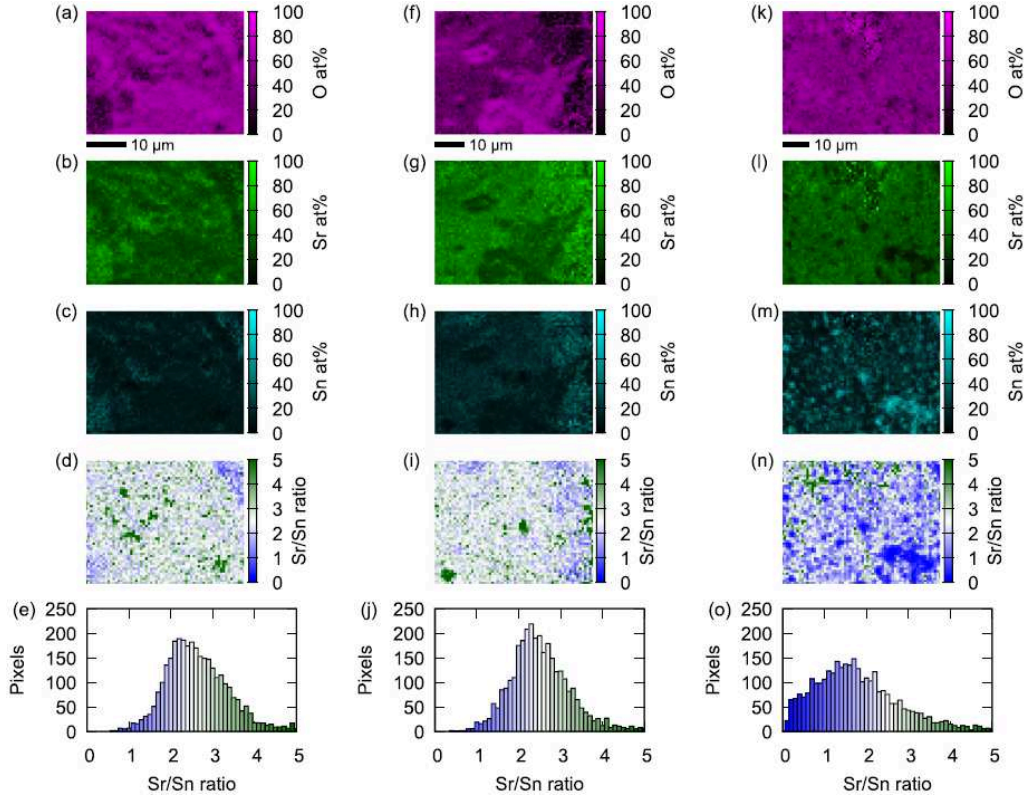

Fig. 2.15 Results of EDX on various $Sr_{3-x}SnO$ samples with a nominal deficiency $x_0 = 0.5$. Spatial mapping of the contents of (a) O, (b), Sr, and (c) Sn in at.%. The amount of oxygen is large because the sample was exposed to air for a few minutes during the transport to the EDX apparatus. (d) Spatial mapping of the Sr/Sn ratio. (e) Distribution of the Sr/Sn ratio shown in a histogram. The panels (f–j) present the same information on a different area of the same batch of the sample. The panels (k–o) present the same information on a different batch of the sample. This figure is reprinted from Ref. [9].

transition temperature is insensitive to x_0 for $0.3 < x_0 < 0.7$. It is also noticeable that even in $0.3 < x_0 < 0.7$, some samples do not show superconductivity. On the other hand, the superconducting volume fraction shown in Figs. 2.16(b) and (c) largely fluctuates with x_0. It is clear in the average volume fraction in Fig. 2.16(d) that the volume fraction has dome-like dependence with the maximum at $x_0 \simeq 0.6$. These features can be understood by the separation into the superconductive and non-superconductive phases within the sample. We expect that the superconductive phase has the actual deficiency $x \simeq 0.6$ and the non-superconductive one has $x \simeq 0$. Depending on the value of x_0, the portion of each phase changes with x

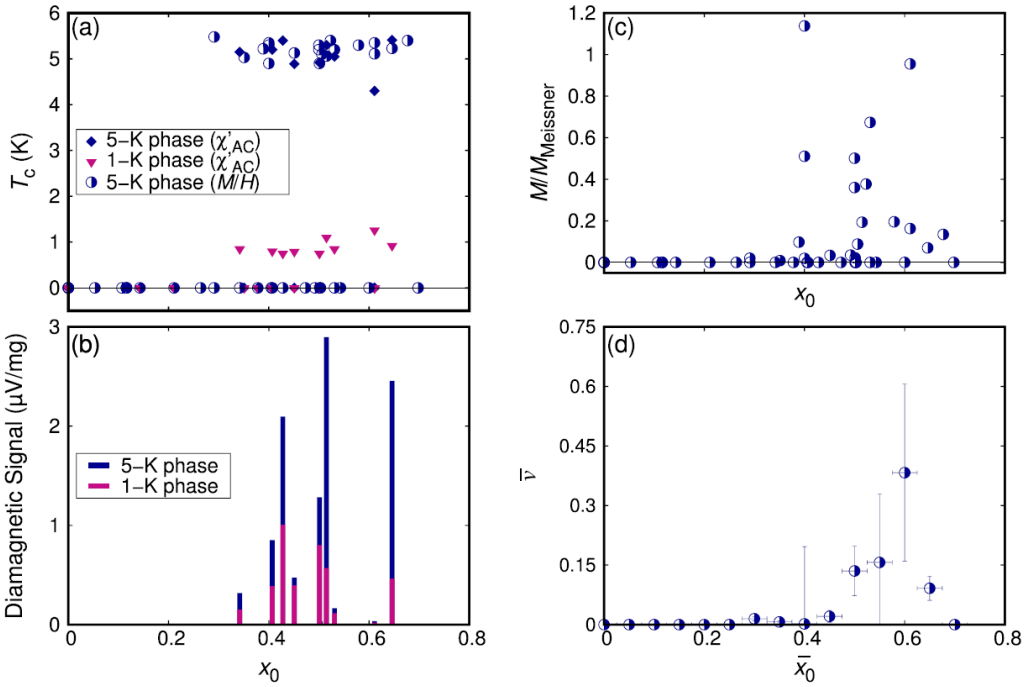

Fig. 2.16 x_0 dependence of (a) the transition temperature measured by AC and DC susceptibility, (b) diamagnetic signal detected by AC susceptibility, (c) shielding fraction deduced from DC susceptibility, and (d) average shielding fraction over 0.05 intervals of x_0. The vertical error bars indicate the weighted standard errors. This figure is reprinted from Ref. [9].

kept at certain values.

The phase splitting is also observed by nuclear magnetic resonance (NMR) [50]. Fig. 2.17(a) shows the NMR spectra of two superconductive and two non-superconductive samples. All the spectra have two peaks suggesting the phase splitting. Since the peak 1 is larger and the peak 2 is almost absent in the non-superconductive samples, we identified the peak 1 from the nearly stoichiometric phase and the peak 2 from the Sr-deficient phase. This interpretation is consistent with the nuclear spin-lattice relaxation rate divided by temperature $1/T_1T$ presented in Fig. 2.17(b). The flat temperature dependence of $1/T_1T$ at the peak 2 is the typical behavior of conventional metals. $1/T_1T$ is proportional to the square of the electronic density of states, and thus $1/T_1T$ close to the Sn metal suggest a large density of states. In contrast, $1/T_1T$ at the peak 1 is 400-times smaller than that at the peak 2. It is also noted that $1/T_1T$ at the peak 1 deviates from the flat temperature dependence at high temperature. This behavior can be explained by assuming that the Fermi energy is located near the

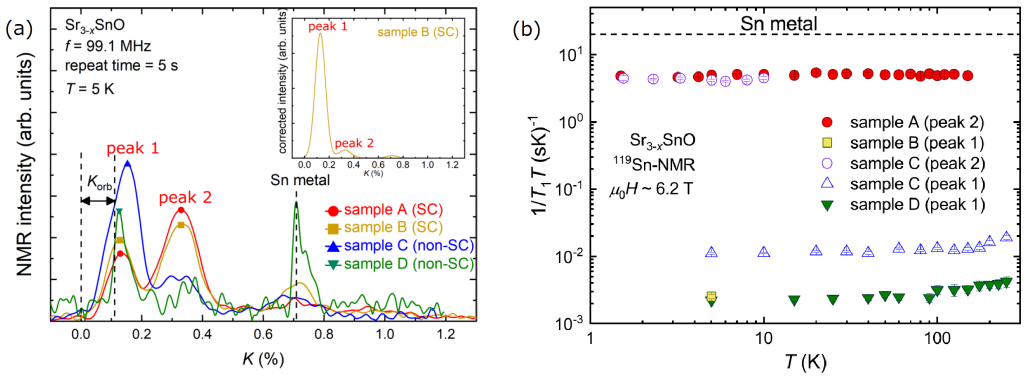

Fig. 2.17 (a) NMR spectra at 5 K for the superconductive (A and B) and non-superconductive (C and D) samples. All the spectra have two peaks, but the peak 1 is larger in the non-superconductive samples than in the superconductive ones. The peak from the Sn impurity observed for Sample D probably originates from a partial decomposition. (b) The nuclear spin-lattice relaxation rate divided by temperature. This figure is reprinted from Ref. [50].

band gap. In order to distinguish whether the band dispersion around the gap is quadratic (conventional semiconductor) or linear (Dirac semimetal), further investigation using the samples with the Fermi energy closer to the band gap is needed.

Since the Mössbauer spectroscopy is applicable to Sn, we measured the ionic state of Sn in $Sr_{3-x}SnO$ and investigated how the spectra changes Sr deficiency. Figure 2.18 shows the Mössbauer spectra of samples with various nominal deficiency x_0. All spectra have strong γ-ray absorption at the same position as Mg_2Sn, in which the Sn^{4-} state is also anticipated. This provided the first spectroscopic evidence of Sn^{4-} in oxides. With Sr deficiency, the samples exhibit additional absorption at 2.59 mm/s. Since the intensity of the additional absorption increases with the amount of Sr deficiency, we expected that this absorption is related to the hole-doped Sn^{4-}. However, microscopic origin was not fully understood or possible β-Sn impurity was nor excluded. In addition, temperature evolution of the Mössbauer spectra was not been reported.

2.2 $CaSb_2$

In 2019, it is reported that $CaSb_2$ has multiple nodal lines in the bulk electronic band structure in the Brillouin zone based on the first-principles calculations (Fig. 2.19) [10]. $CaSb_2$ crystallizes in a non-symmorphic structure with the space group $P2_1/m$ (No. 11, C_{2h}^2). The screw and mirror symmetries protect the nodal

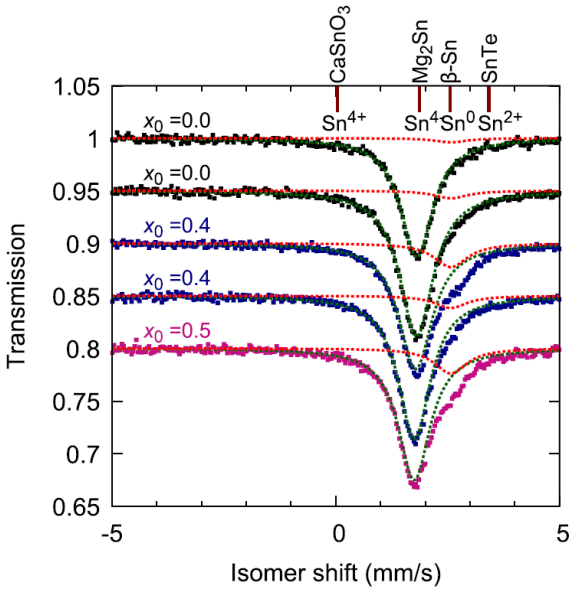

Fig. 2.18 Mössbauer spectra for samples with various nominal Sr deficiency x_0. The Sn^{4-} state was observed for all samples. This figure is reprinted from Ref. [9].

line via the zero-dimensional topological invariant

$$N\left(k_x, k_y\right) = \sum_{n=1}^{M} \langle \left(k_x, k_y, \frac{\pi}{b}\right) n|im| \left(k_x, k_y, \frac{\pi}{b}\right) n\rangle \,, \tag{2.1}$$

where $|(k_x, k_y, \frac{\pi}{b})n\rangle$ is the nth band, m is the mirror operation. We comment here that the authors chose k_z to be along the b^* direction. Since the screw rotation anticommutes with the mirror reflection on the $k_z = \pi/b$ plane, we obtain $N(k_x, k_y) = -N(-k_x, -k_y)$. This relation requires odd numbers of gap closing between $(k_x, k_y, \pi/b)$ and $(-k_x, -k_y, \pi/b)$ when $N(k_x, k_y)$ is odd. Thus, there exist nodal lines on the $k_z = \pi/b$ plane as illustrated in Fig. 2.20. This nodal line is robust against the spin-orbit interaction.

In the absence of the spin-orbit coupling, many materials can host nodal lines originating from band crossings. However, without any additional symmetry such as non-symmorphic symmetry that protects the nodal lines, nodal lines are generally gapped out by the spin-orbit coupling and the material turns into an insulator or a point-nodal semimetal [32, 51]. Therefore, only a few materials are proposed to be line-nodal materials in the presence of the spin-orbit coupling so far [52–55]. Superconductivity in such materials with nodal lines stable against the spin-orbit interaction is even more limited [25].

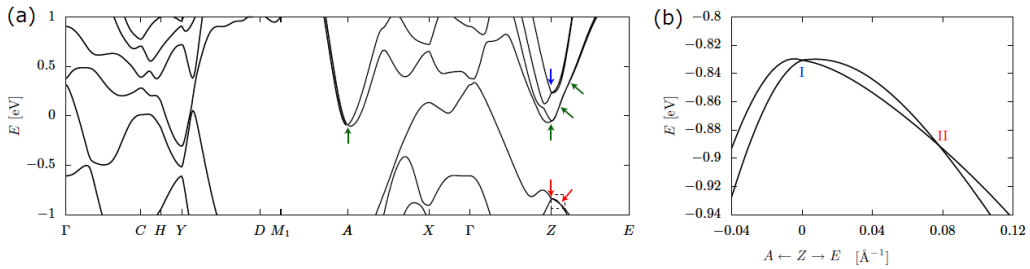

Fig. 2.19 (a) Band structure of $CaSb_2$ with the spin-orbit coupling. The arrows indicate the positions of some nodal lines. (b) Magnified view of the nodal line pointed by the red arrows in the panel (a). One of the two Dirac cones is type-I and the other is type-II. This figure is reprinted from Ref. [10].

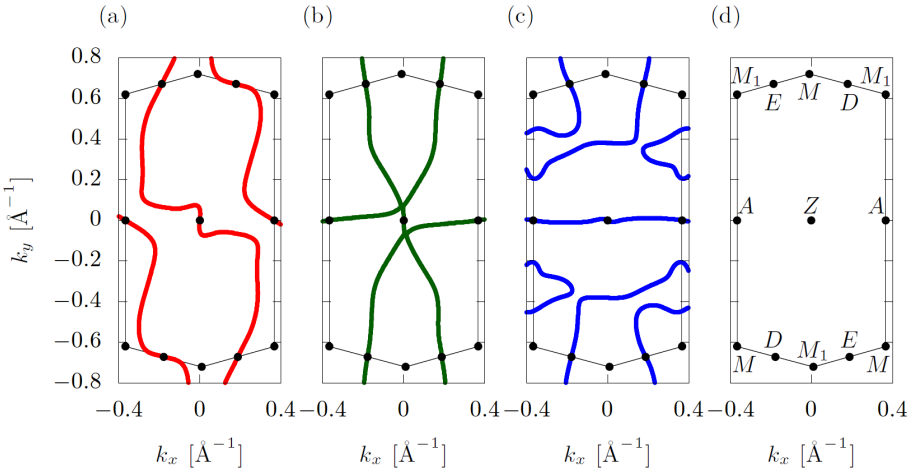

Fig. 2.20 Nodal lines at the (a) lowest, (b) intermediate, and (c) highest bands presented in Fig. 2.19. This figure is reprinted from Ref. [10].

Chapter 3

Experiment

3.1 Sample syntheses

Polycrystalline samples of $Sr_{3-x}SnO$ were synthesized using the reaction $(3-x_0)Sr + SnO \longrightarrow Sr_{3-x}SnO + (x-x_0)Sr\uparrow$. Here, x_0 is the nominal value of the Sr deficiency. All the reactants and products were treated in a glovebox filled with argon in order to prevent decomposition. The samples for high-energy x-ray diffraction (XRD) was synthesized from Sr (Sigma-Aldrich, 99.99%) and SnO (Furuuchi, 99.9%) with $x_0 = 0.5$ in an alumina crucible (IRIE Corporation, SSA-S) by Method B described in Table 2.1 using a box furnace (Denken, KDF 80S).

The $Sr_{3-x}SnO$ samples for Mössbauer spectroscopy were synthesized from Sr (Sigma-Aldrich, 99.99%) and SnO (Sigma-Aldrich, 99.99%) in iron crucibles (Chiyoda Kogyo Seisakusho). The nearly stoichiometric (NS) sample has the excess Sr of $x_0 = -0.5$ because the sample with $x_0 = 0$ contained SrO impurity. The crucible was sealed in a stainless-steel capsule (Fujikin, SUS316L pipe, ϕ19.05×1.65t×110 mm sealed with Fujikin, V-LOK Cap, VUWJC-19.05) under 1 atm of argon at room temperature. The capsule was heated up to 1000°C over 10.5 h, kept there for 50 h, and cooled down to 800°C in 6 h. The capsule was kept at 800°C for 20 h, and then cooled down to room temperature in 8 h [44]. We also prepared the Sr-deficient (D) sample with $x_0 = +0.5$. The crucible was sealed in a quartz tube under 0.3 atm of argon at room temperature. The tube was heated up to 850°C over 3 h, kept there for 3 h, and quenched in water. Subsequently the tube was heated at 600°C for 48 h followed by furnace cooling. Although the actual amount of deficiency x was not measured, we expect $x \simeq x_0$ in the D sample because the evaporated Sr was estimated to be only 0.2% judgin from the difference in the mass before and after heating. In the case of the NS sample, some amount of Sr seemed to stick on the crucible. Energy dispersive x-ray spectroscopy (EDX) indicates Sr/Sn = 2.98 (i.e. $x = 0.02$) for a sample

synthesized under a condition similar to that of the NS sample. Thus, we expect $x \simeq 0$ in the NS sample. As mentioned in Chapter 2, spontaneous deficiency of Ca is reported in Ca_3PbO. The amount of Ca deficiency was reported to be $x = 0.06$ by electron-probe microanalysis.

We synthesized three $Sr_{3-x}SnO$ samples for μSR measurements from Sr (Sigma-Aldrich, 99.99%) and SnO (Sigma-Aldrich, 99.99%) in alumina crucibles by Method B. According to the powder XRD (PXRD), the samples were mainly $Sr_{3-x}SnO$ with the lattice parameters of $a = 0.51429(4)$ nm in Sample A, $a = 0.51435(3)$ nm in Sample B, and $a = 0.51421(4)$ nm for Sample C. The sample for the specific-heat measurement (Sample D) was synthesized by Method A from the stoichiometric ratio of Sr (Furuuchi, 99.9%) and SnO (Furuuchi, 99.9%).

A polycrystalline sample of $CaSb_2$ was synthesized from Ca (Sigma-Aldrich, 99.99%) and Sb (Rare Metallic, 99.99%). The stoichiometric ratio of the reactants was placed in an alumina crucible under argon atmosphere. The crucible was sealed in a quartz tube under 0.2 atm of argon at room temperature. The tube was heated up to 1000°C over 3 h, kept there for 24 h, and quenched in water in order to prevent the phase splitting into $Ca_{11}Sb_{10}$ and Sb [56]. The sample was ground, pelletized, and sealed in a quartz tube under 0.3 atm of argon. The tube was heated to 550°C over 2 h and kept for 48 h followed by furnace cooling. The second annealing temperature was below the $CaSb_2$-Sb eutectic temperature 587°C. After the second annealing, the sample was handled in air. We comment that a method similar to the previously reported one, starting from a molar ratio of Ca:Sb = 1:3.9 and slow cooling from 700°C [10], resulted in a sample containing a lot of Sb side product, whose amount is larger than the target product $CaSb_2$.

3.2 X-ray diffraction

High-energy XRD measurements were performed at the beamline BL02B2 in the synchrotron facility SPring-8 using a Debye-Scherrer camera. The wavelength of the incident beam was calculated to be 0.042073 nm using CeO_2 as a standard reference. Sample was sealed in a quartz tube under nitrogen atmosphere in order to prevent decomposition of $Sr_{3-x}SnO$.

Laboratory PXRD patterns were collected with the Cu-$K\alpha$ radiation (wavelengths of 0.1540538 nm for $K\alpha_1$ and 0.1544324 nm for $K\alpha_2$) using a commercial diffractometer (Bruker AXS, D8 Advance) equipped with an array of 192 detectors. The diffracted X ray was integrated over 0.3 s for each angle, and the total measurement time was approximately 30 minutes for each sample. When we measured $Sr_{3-x}SnO$, we covered the sample and the glass stage with a polyimide film (DuPont-Toray, Kapton 50H; thickness of 12.5 μm) fixed with vacuum grease (Dow

Corning Toray, High-Vacuum Grease) under argon atmosphere.

3.3 Magnetic susceptibility

Direct-current (DC) magnetization was measured with a commercial magnetometer using a superconducting quantum interference device (Quantum Design, MPMS-XL). For $Sr_{3-x}SnO$, polycrystalline samples were placed inside thin plastic capsule under an argon atmosphere. For $CaSb_2$, we used a ^{3}He refrigerator (IQUANTUM, iHelium3) for MPMS.

Alternating-current (AC) magnetic susceptibility was measured with a lock-in amplifier (Stanford Research Systems, SR830) using a miniature susceptometer [57] compatible with an adiabatic demagnetization refrigerator (ADR) of a commercial apparatus (Quantum Design, PPMS). Sintered chunks of $Sr_{3-x}SnO$ used for AC susceptibility measurements were covered with grease (Apiezon, N grease) to avoid direct contact to air.

3.4 Electrical transport

The electrical resistivity of $CaSb_2$ was measured by a standard four-probe method using the ADR option of PPMS. Gold wires with a diameter of 25 μm (Tanaka Denshi Kogyo, 99.99%) were attached to the pellet using room-temperature-cure silver paste (DuPont Electronics Material, 4929N) with n-butyl acetate (nacalai tesque, 99.0%) as solvent. We comment that zero resistance was not observed when we used silver epoxy (Epoxy Technology, H20E), possibly because the sample reacted with air or with the silver epoxy during the curing process at 120°C.

3.5 Heat capacity

Heat capacity was measured using a calorimeter for a ^{3}He option of PPMS, by using the relaxation method. Samples were fixed on the stage with a thin layer of grease (Apiezon, N-grease) to obtain good thermal connection. In the case of $Sr_{3-x}SnO$, a sintered chunk with a mass of 13.3 mg was used. In the case of $CaSb_2$, a cut pellet with a mass of 15.7 mg (approximately $2 \times 2 \times 1$ mm^3) was measured For each measurement, a heat pulse raised the sample temperature by 3% of the bath temperature and the temperature relaxation curve was fitted using a double exponential function to evaluate the heat capacity.

3.6 Mössbauer spectroscopy

Figure 3.1(a) depicts the setup of Mössbauer spectroscopy. We prepare a radioisotope as a γ-ray source and detect the transmission through the sample. By oscillating the γ-ray source, we can change the energy of γ ray via Doppler effect. Typical Mössbauer spectra are shown in Fig. 3.1(b). The sample absorb a γ ray having the excitation of the Sn nucleus in the sample. The excitation energy of the nucleus is affected by the surrounding electrons, and the isomer shift (IS; velocity of the γ-ray source when absorption occurs) can be expressed as

$$\mathrm{IS} = K(\langle R_\mathrm{e}^2\rangle - \langle R_\mathrm{g}^2\rangle)([\Psi_s^2(0)]_\mathrm{sample} - [\Psi_s^2(0)]_\mathrm{source}), \tag{3.1}$$

where K is a nuclear constant, $\langle R_\mathrm{e}^2\rangle - \langle R_\mathrm{g}^2\rangle$ is the difference of the effective nuclear charge radius between the excited and ground states, and $\Psi_s^2(0)$ is the electronic density at the nucleus position [58]. It is known that the Sn nucleus has a larger effective radius in the excited state than in the ground state. Therefore, a larger electronic density leads to a larger isomer shift. Since s electrons have non-zero density at the nucleus position, more s electrons result in a larger isomer shift. In contrast, since p and d electrons expel s electrons via screening effect, more p and d electrons slightly push the isomer shift to the smaller side.

From the temperature dependence of the absorption, we can deduce the Debye temperature. The intensity of the absorption is proportional to the recoil-free fraction

$$f = \exp\left(-\frac{(2\pi)^2 \langle r^2\rangle_\mathrm{D}}{\lambda^2}\right), \tag{3.2}$$

$$\langle r^2\rangle_\mathrm{D} = \frac{3\hbar^2}{M k_\mathrm{B}\Theta_\mathrm{D}}\left[\frac{1}{4} + \left(\frac{T}{\Theta_\mathrm{D}}\right)^2 \int_0^{(\Theta_\mathrm{D}/T)} \frac{y\mathrm{d}y}{\mathrm{e}^y - 1}\right], \tag{3.3}$$

where $\langle r^2\rangle_\mathrm{D}$ is the mean square displacement in the Debye solid, $\lambda = 0.51933$ nm is the wavelength of the γ ray, $\hbar$ is the reduced Planck constant, M is the mass of a ^{119}Sn atom, k_B is the Boltzmann constant, and Θ_D is the effective Debye temperature (or Mössbauer temperature) characterizing the vibrations of the Sn atoms [60]. At $T \ll \Theta_\mathrm{D}$, f is reduced to

$$f = \exp\left(-\frac{(2\pi)^2 3\hbar^2 T}{M k_\mathrm{B}\lambda^2\Theta_\mathrm{D}^2}\right). \tag{3.4}$$

Therefore, the absorption decreases if we increase temperature. At high temperature, rapid thermal vibration of the Sn nucleus changes the energy of the γ ray via the second-order Doppler shift, and thus the absorption is suppressed.

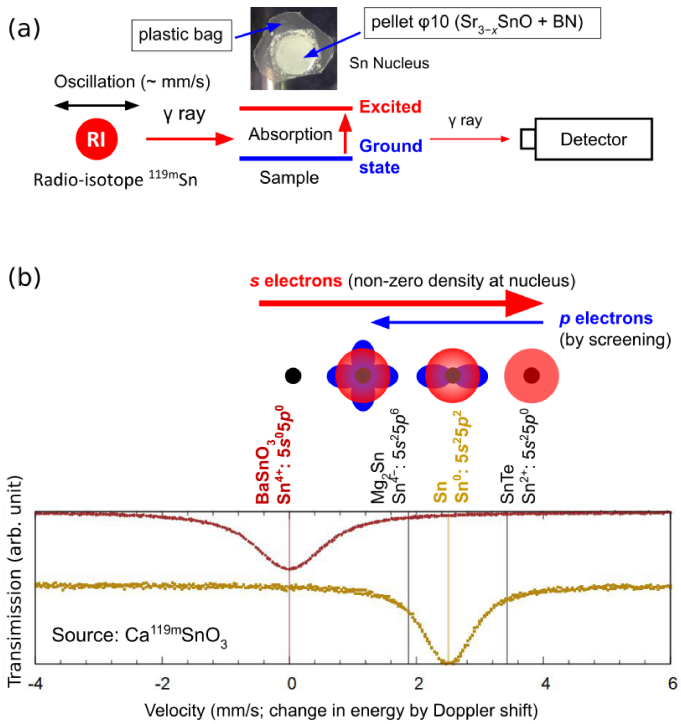

Fig. 3.1 (a) Schematic image of the setup of Mössbauer spectroscopy. (b) Typical Mössbauer spectra. Reported isomer shifts of Mg_2Sn and SnTe [59] are also presented.

We used ^{119m}Sn contained in $CaSnO_3$ (Ritverc GmbH, 740 MBq) the γ-ray source. The velocity of the source was calibrated using the absorptions of ^{57}Fe, and its origin (corresponding to $[\Psi_s^2(0)]_{\mathrm{source}}$) was set to the isomer shift of $BaSnO_3$ at room temperature. A palladium film with the thickness of 75 μm was placed in front of the sample in order to shut the X-ray fluorescence of tin. After the magnetic measurements, the sample powder (around 40 mg) was taken out from the capsule and mixed with boron nitride (Kishida Chemical, 99.5%; approximately 70 mg) and polyethylene (Beckman RIIC, polyethylene powder for IR spectroscopy; approximately 8 mg) powders in a glovebox filled with nitrogen in order to improve the spatial homogeneity of the sample. Then the sample was pressed into a pellet with a diameter of 10 mm and sealed in multiple layers of polyethylene bags with the thickness of 0.1 mm in order to avoid direct contact to air. All the measurements, from room temperature to below 3 K, were carried out inside a ^{4}He cryostat (Janis Research, ST-400). Typical measurement time was 12 hours at each temperature.

3.7 Muon spin spectroscopy

Figure 3.2(a) is a schematic image of the μSR experiment. We shoot spin-polarized muon μ^+ to the sample under magnetic field. μ^+ decays into a positron e^+, and e^+ is emitted in the direction of the spin of μ^+. Thus, if we detect e^+ with two detectors, we observe a oscillation of the difference in count (called asymmetry A) reflecting the Larmor oscillation of μ^+ spin as shown in Fig. 3.2(b). In type-II superconductors in the vortex state, there is a distribution of the flux density inside the sample. Therefore, μ^+ at different position feels different field. Then, we observe a superposition of Larmor oscillations with various frequencies, resulting in the dumping of the oscillation amplitude. Assuming the Gaussian distribution for the probability $n(B)$ that a muon stops at a position with a local flux density of B, we obtain the Gaussian cosine function

$$A(t) = A(0) \exp\left(-\frac{\sigma^2 t^2}{2}\right) \cos\left(2\pi\gamma_\mu B_0 t + \phi\right), \tag{3.5}$$

where $A(0)$ and ϕ are the asymmetry and phase at $t = 0$, respectively, γ_μ is the gyromagnetic ratio of muon, and B_0 is the mean flux density inside the sample. The relaxation rate σ is related to the London penetration depth $\lambda(T)$ as

$$\sigma_{\mathrm{SC}}(T) = \sqrt{0.00371} \times \frac{2\pi\gamma_\mu \Phi_0}{\lambda^2(T)}, \tag{3.6}$$

where $\sigma_{\mathrm{SC}}(T) = \sqrt{\sigma^2(T) - \sigma_{\mathrm{N}}^2}$ is the increase of the relaxation rate due to superconductivity, σ_{N} is the relaxation rate in the normal state mostly attributable to the nuclear contribution, and Φ_0 is the flux quantum [61]. We can investigate the presence of the time-reversal symmetry by zero-field μSR. If σ changes at a certain temperature under zero field, there is a spontaneous field in the sample, or time-reversal symmetry is broken.

For μSR, we used pellets with a diameter of 10 mm. Measurements on Sample A were performed at the GPS spectrometer (πM3 beamline) at the Paul Scherrer Institute (PSI) down to 1.5 K. The pellet was sealed in a polyethylene bag with a thickness of 0.1 mm under argon atmosphere in order to avoid direct contact to air. All data are available in the following web site `http://musruser.epsi.ch/cgi-bin/SearchDB.cgi` with the key words *Area*: GPS, *Year*: 2018, and *Run Title*: Sr2p5SnO. Measurements on Samples B and C were carried out at the Dolly spectrometer (πE1 beamline) at PSI down to 0.26 K. Sample pellets were placed on Cu foils with a thickness of 25 μm with grease (Apiezon, N Grease) under nitrogen atmosphere to achieve a good thermal contact. Then the sample

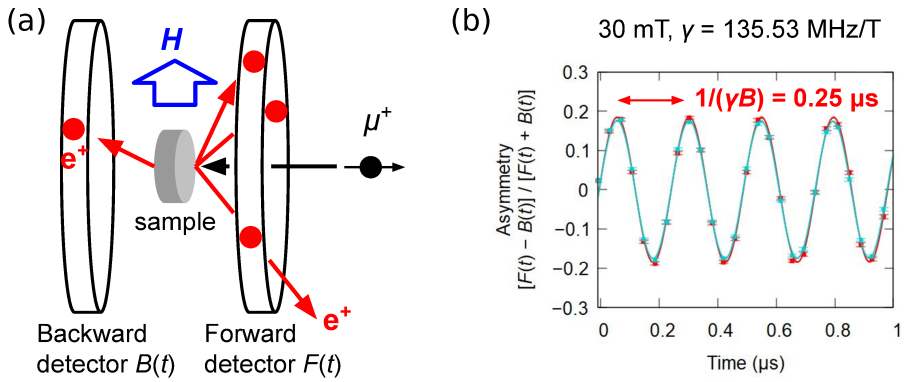

Fig. 3.2 (a) Schematic image of the setup of μSR. (b) Typical μSR signal asymmetry, showing a clear Larmor oscillation.

was sealed with a polyimide film (Du Pont, Kapton). The pellets of Samples B and C were mounted on the cryostat using a portable glovebox with continuous flow of nitrogen. All data are available in the above database with the key words *Area*: Dolly, *Year*: 2019, and *Run Title*: Sr2p5SnO. The typical integration time of μSR was 1.5 h for each temperature and field condition.

3.8 First-Principles Calculation

We calculated the band structure of $Sr_{3-x}SnO$ with two programs: WIEN2k [62], which uses full-potential linearized augmented plane wave plus local orbitals method, and AkaiKKR (also called Machikaneyama) [63], using the Korringa-Kohn-Rostoker Green function method [64, 65]. In both packages, we used the Perdew-Burke-Ernzerhof generalized gradient approximation [66] as the exchange-correlation functional and took the spin-orbit coupling into account. We assumed the paramagnetic state for both stoichiometric and deficient phases. The experimentally reported crystalline structure [44] was used for the calculation of Sr_3SnO. Figures 3.3(a) and (d) show the crystalline structure and the Brillouin zone of Sr_3SnO.

In the case of WIEN2k, the radius R of the muffin-tin sphere of each atom was set to $R_{\mathrm{Sr}} = R_{\mathrm{O}} = 2.39a_{\mathrm{B}}$ and $R_{\mathrm{Sn}} = 2.5a_{\mathrm{B}}$, where a_{B} is the Bohr radius. We set the plane-wave cut off $RK_{\mathrm{max}} = 7$, the highest angular momentum $l_{\mathrm{max}} = 10$, maximum magnitude of the largest vector in charge density Fourier expansion $G_{\mathrm{max}} = 12$, and separation energy between the valence and core states -6.0 Ry. To see the effect of the strontium deficiency, we calculated the band structures of two hypothetical superstructures with different patterns of the deficiency, shown in Figs. 3.3(b) and (c). In the structure shown in Fig. 3.3(b), strontium atoms

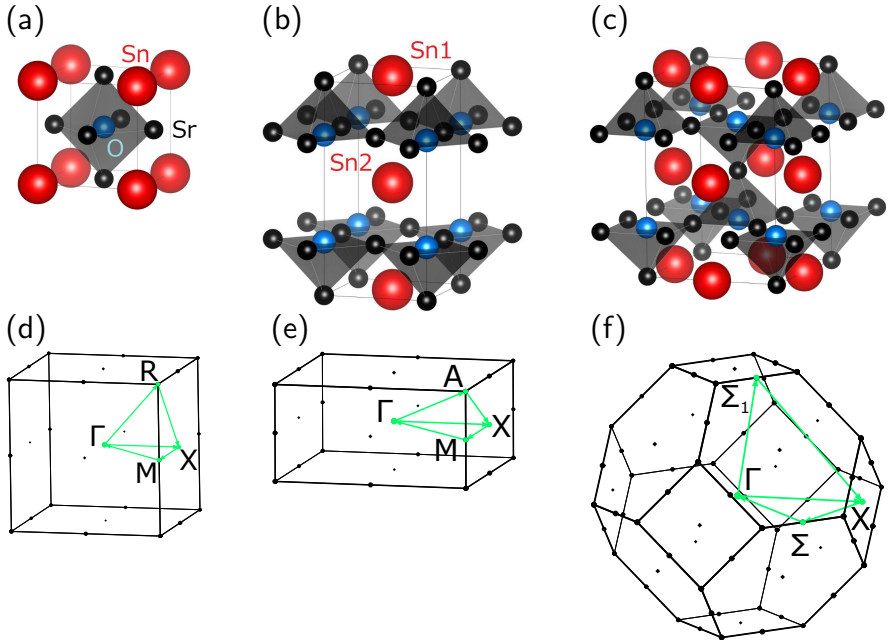

Fig. 3.3 (a) Crystalline structure of Sr_3SnO. The black, red, and blue spheres represent the Sr, Sn, and O atoms, respectively. (b, c) Hypothetical structures of strontium-deficient $Sr_{2.5}SnO$. The structure (b) has the layers of the strontium deficiency resulting in a simple tetragonal lattice with the space group $P4/mmm$ (No. 124, D^1_{4h}). On the other hand, in the structure (c), the strontium atoms are vacant alternatively from different layers, resulting in a body-centered tetragonal lattice with the space group $I4/mmm$ (No. 139, D^{17}_{4h}). The figures of the crystal structures were prepared with the program VESTA [67]. Brillouin zones of the (d) simple cubic, (e) simple tetragonal, and (f) body-centered tetragonal lattices. The k paths for the band-structure plots in Figs. 4.2 and 4.3 are indicated. The figures of the Brillouin zones were drawn with the program XCrySDen [68].

in certain layers are missing. In the structure of Fig. 3.3(c), strontium atoms are taken away alternatively from two neighboring layers. k meshes of $10\times10\times10$ were used for the calculation of Sr_3SnO and the body-centered tetragonal $Sr_{3-x}SnO$ [Fig. 3.3(c)] and $10 \times 10 \times 5$ for the simple-tetragonal $Sr_{3-x}SnO$ [Fig. 3.3(b)]. Figures 3.3(e) and (f) show the Brillouin zones of the simple and body-centered tetragonal lattices.

When using AkaiKKR, the muffin-tin radii R of all atoms were set to $R_{\mathrm{Sr}} = R_{\mathrm{Sn}} = R_{\mathrm{O}} = a/4$, where a is the lattice parameter. We set the small imaginary part of the energy $E_{\mathrm{delt}} = 0.0003$ Ry and separation energy between the valence and core states $E_{\mathrm{width}} = 1.9$ Ry. A k mesh of $8\times8\times8$ was used for the calculation

of Sr_3SnO and $Sr_{3-x}SnO$. For the calculation of $Sr_{3-x}SnO$, we used the coherent potential approximation [69,70], which allows us to calculate randomly disordered systems.

To analyze the Mössbauer spectra of $Sr_{3-x}SnO$, too, we performed first-principles calculations. Here, we calculated electronic densities of various Sn-based materials including $Sr_{3-x}SnO$ in order to deduce the relation between the electronic density and the isomer shift. The density of electrons at the Sn nucleus position was calculated with WIEN2k. We chose $R_{\mathrm{Sr}} = R_{\mathrm{O}} = 2.41a_{\mathrm{B}}$ and $R_{\mathrm{Sn}} = 2.5a_{\mathrm{B}}$. We used finer parameters of $RK_{\max} = 8$, $G_{\max} = 18$, and the separation energy of -7.0 Ry [71]. Only when estimating the energy of the local lattice vibrations in the hypothetical superstructure "$Sr_2Sn_2O_2$," did we use the separation energy of -6.0 Ry in order to avoid a technical problem. The Inorganic Crystal Structure Database (ICSD) numbers of the experimentally reported structures and the sizes of the k mesh used for calculations were 78894 and $12 \times 12 \times 12$ for SnF_4, 239582 and $12 \times 12 \times 12$ for $BaSnO_3$, 411242 and $10 \times 15 \times 10$ for $SnCl_4$, 43594 and $14 \times 14 \times 7$ for $SnSe_2$, 642850 and $12 \times 12 \times 12$ for Mg_2Sn, 40038 and $12 \times 12 \times 12$ for β-Sn, 186650 and $6 \times 17 \times 16$ for SnSe, 15452 and $10 \times 18 \times 8$ for $SnCl_2$. The calculated electronic densities of these compounds were compared with the experimentally observed isomer shifts [59,72]. For Sr_3SnO, we used the structure reported by J. Nuss *et al.* [44] and the k mesh of $12 \times 12 \times 12$. For strontium-deficient $Sr_{3-x}SnO$, hypothetical structures based on Sr_3SnO ("$Sr_4Sn_2O_2$," "$Sr_3Sn_2O_2$," and "$Sr_2Sn_2O_2$," see Fig. 3.4; k mesh of $12 \times 12 \times 6$) were assumed.

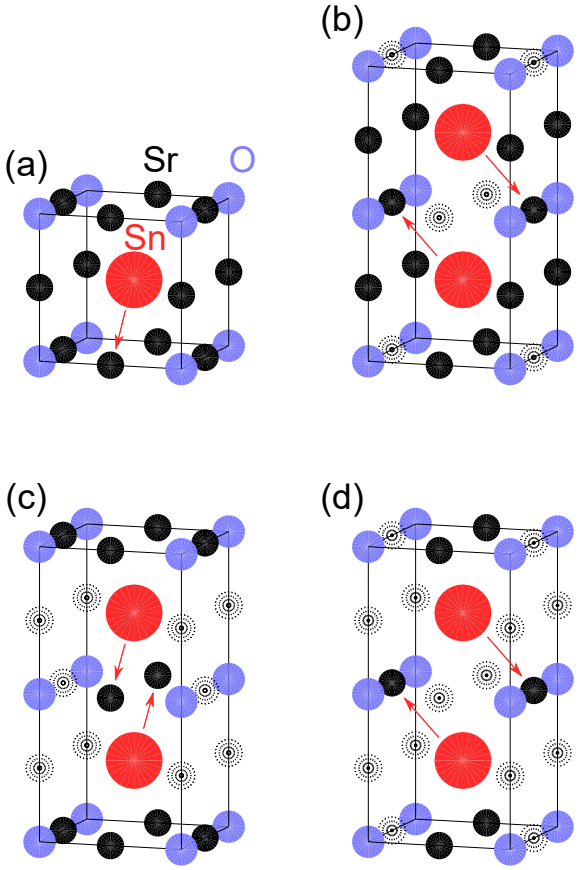

Fig. 3.4 (a) Crystalline structure of Sr_3SnO. In contrast to the common picture with the OSr_6 octahedron shown at the center, Sn (red sphere) is placed at the center of the unit cell in this picture. (b)–(d) Three hypothetical structures of highly Sr-deficient antiperovskite oxides (b) "$Sr_4Sn_2O_2$," (c) "$Sr_3Sn_2O_2$," and (d) "$Sr_2Sn_2O_2$." The dotted spheres indicate the assumed positions of the Sr deficiency. The arrows indicate the direction of the atomic shift for calculation of the force constants of Sn vibrations. The figures were prepared with the program VESTA [67].

Chapter 4

Band structure calculation of $Sr_{3-x}SnO$

In this chapter, we present the results of high-energy XRD and the band structure of $Sr_{3-x}SnO$ obtained by first-principles calculations, revealing a heavy hole doping compared to the band-inverted energy region. The contents in this chapter is based on Ref. [1].

4.1 High-energy XRD

First, we present in Fig. 4.1 the high-energy PXRD pattern, together with simulations for SrO, stoichiometric Sr_3SnO, and two hypothetical $Sr_{2.5}SnO$ structures. The experimental pattern basically matches with the simulation for Sr_3SnO. Nevertheless, the experimental pattern exhibits clear phase splitting evidenced by the double peaks shown in the right panel. We consider that the minor phase is SrO (face-centered cubic, space group $Fm\bar{3}m$, No. 225, O_h^5) for the following two reasons. First, the peak at 6.6° does not split. Because only Sr_3SnO has a peak at 6.6°, this absence of the splitting means that there is only one Sr_3SnO phase in the sample. Second, while the peak around 8.2° has larger intensity than the one around 9.4° in the simulation for Sr_3SnO, the peak at 9.4° is higher in SrO. The major and minor phases in the observed spectrum have the same tendency as Sr_3SnO and SrO, respectively. These data suggest that the sample consists of $Sr_{3-x}SnO$ as the major phase and SrO as a minor one. From the positions of some sharp peaks, the cell parameters a of the major and minor phases were evaluated to be 0.512152 ± 0.000010 nm and 0.51495 ± 0.00004 nm, respectively, where the errors represent the standard errors of the least square fittings. These values are consistent with the reported cell parameters $a = 0.51394$ nm [44] for Sr_3SnO and $a = 0.51615$ nm [73] for SrO. No clear peaks originating from the superstruc-

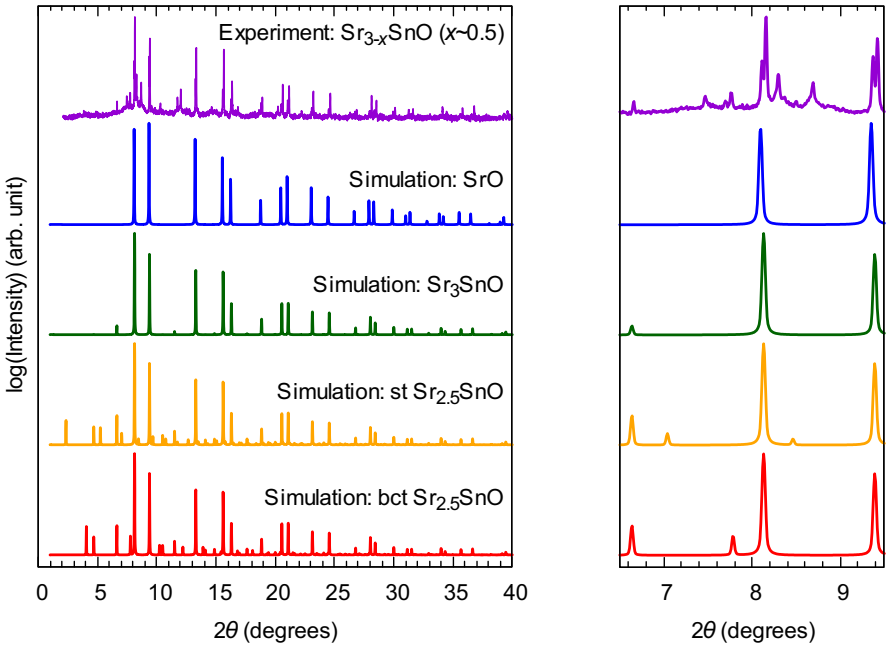

Fig. 4.1 Experimental and theoretical PXRD patterns of $Sr_{3-x}SnO$ and SrO. The purple one is the experimental data for the superconductive $Sr_{3-x}SnO$ ($x \sim 0.5; T_c \sim 5.2$ K) measured at 30 K and at SPring-8. The blue, green, yellow, and red ones are the simulated patterns for SrO, Sr_3SnO, the simple-tetragonal (st) $Sr_{3-x}SnO$ ($x = 0.5$) shown in Fig. 3.3(b), and the body-centered-tetragonal (bct) $Sr_{3-x}SnO$ ($x = 0.5$) shown in Fig. 3.3(c), respectively. The patterns were calculated using VESTA [67].

tures were observed below $2\theta = 7°$, suggesting that the strontium deficiencies are randomly distributed. Although in the high angles there are some peaks which coincide with the superlattice peaks, we consider that they are attributable to impurities.

4.2 Band-structure calculations

Figures 4.2 (a) and (b) show the energy bands of Sr_3SnO calculated using WIEN2k and AkaiKKR, respectively, without spin-orbit coupling. Two programs produce similar band structures with Dirac cones along the Γ-X line. It is noticeable that the bands are metallic because of the valence bands exceeding the Fermi energy at the Γ point. Figures 4.2(c) and (d) are the energy dispersions calculated with spin-orbit coupling. Although the overall shapes of the bands are roughly consistent between the two packages, there are some detailed differences. First, while

WIEN2k shows a semiconducting band structure with a slight gap of 0.039 eV, AkaiKKR retains a metallic structure. According to the tight-binding model [5] for Ca_3PbO, another antiperovskite oxide with the band inversion, the valence bands basically originate from the Sn-5p orbitals with the total angular momentum $j = 3/2$. Among the $j = 3/2$ states, only the $j_z = \pm 1/2$ states are energetically lowered by the band repulsion with the conduction bands while the $j_z = \pm 3/2$ states form the Dirac cone because of the suppression of the repulsion by the crystalline and orbital symmetries. This band repulsion between the $j_z = \pm 1/2$ states and the conduction bands, or the effect of the spin-orbit interaction of tin, seems smaller in AkaiKKR than in WIEN2k, resulting in the metallic band structure in the latter. The discrepancy likely originates from the two programs using different calculation methods. Since nonmetallic temperature dependence of the resistivity is experimentally observed for stoichiometric Sr_3SnO [7,74,75], the band structure obtained by WIEN2k should be closer to the reality. The second difference is that the band structure by WIEN2k has two four-fold degeneracies above and below the Fermi energy at the Γ point while the band structure by AkaiKKR lifts the degeneracy above the Fermi energy. This may be because AkaiKKR does not take account of the symmetries in the space group whereas WIEN2k does.

Figure 4.3 shows the dispersion relations of $Sr_{3-x}SnO$ calculated using WIEN2k and AkaiKKR with the spin-orbit interaction. We adopted the coherent potential approximation in Fig. 4.3(c) to take account of the random deficiency evidenced by the PXRD measurement. In all calculations, reflecting the hole doping by the strontium deficiency, the Fermi energy is located at around 0.8 eV below the trace of the Dirac cone. Though the two programs predict different amount of repulsion between the valence and conduction bands, such a difference around the original Fermi energy of Sr_3SnO does not affect much to the properties of heavily doped $Sr_{3-x}SnO$ ($x \sim 0.5$). This amount of lowering of the Fermi energy is consistent with the expected value from the rigid-band shift of Fig. 4.2. In fact, considering the number of the carriers, the rigid-band shift of Figs. 4.2(c) and (d) gives Fermi energies of -0.9 eV and -0.8 eV for $Sr_{2.5}SnO$, respectively. Since the band inversion in Sr_3SnO occurs down to about -0.06 eV in Fig. 4.2(c) and to -0.16 eV in Fig. 4.2(d), p-d mixing necessary to the topological crystalline superconductivity is considered to be small in $Sr_{3-x}SnO$ with $x \sim 0.5$. Naively, for the topological crystalline superconductivity, hole doping which shifts the Fermi energy by 0.06 eV with respect to Fig. 4.2(c) or by 0.16 eV with respect to Fig. 4.2(d) will be favorable, which corresponds to $x = 0.0002$ or $x = 0.01$ assuming the rigid-band shift.

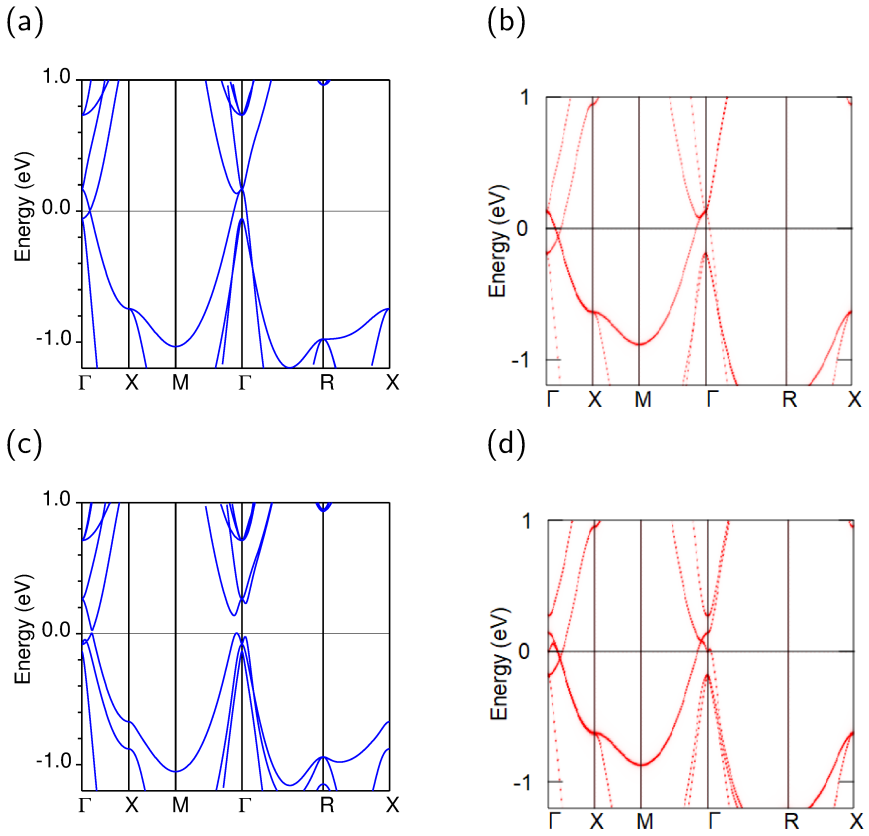

Fig. 4.2 (a, c) Band structures of Sr_3SnO calculated using WIEN2k [62] excluding and including spin-orbit interactions, respectively. (b, d) Bloch spectral functions of Sr_3SnO calculated using AkaiKKR (Machikaneyama) [63] excluding and including spin-orbit interactions, respectively.

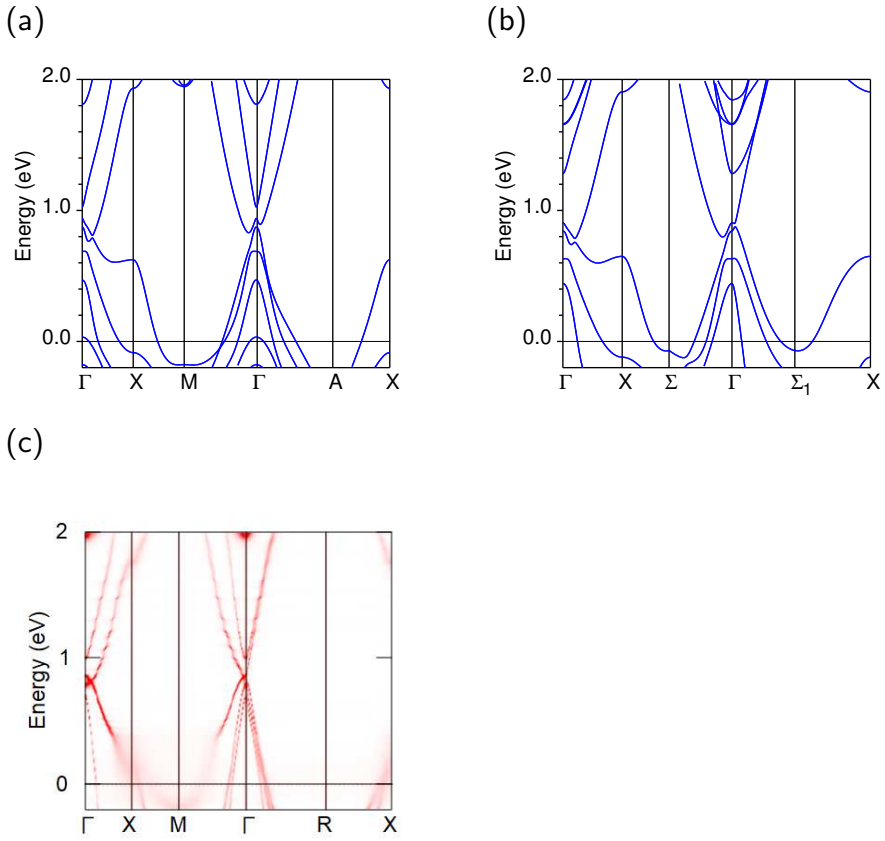

Fig. 4.3 Band structures of $Sr_{3-x}SnO$ ($x \sim 0.5$) calculated using (a, b) WIEN2k [62] and (c) AkaiKKR (Machikaneyama) [63]. The panels (b) and (c) correspond to the hypothetical deficient structures presented in Figs. 3.3(a) and (b), respectively. (c) is the Bloch spectral function calculated using the coherent potential approximation [69, 70] with a strontium deficiency of 17% ($x = 0.51$). In the blurred region, states have finite lifetime because of the scattering by the random deficiency.

Chapter 5

Hole-doped anionic states of Sn in $Sr_{3-x}SnO$ revealed by Mössbauer spectroscopy

In this chapter, we present the temperature dependence of the Sn-Mössbauer spectra for the nearly stoichiometric and Sr-deficient $Sr_{3-x}SnO$ samples. Both samples exhibit two Sn states; Sn^{4-} characteristic of antiperovskite oxides and the other with a higher isomer shift particularly visible in the deficient sample. Detailed analyses of the temperature dependent spectra show that the additional Sn state has a smaller number of electrons and lower energy of the local lattice vibrations. We also performed the first-principles calculations on various hypothetical Sr-deficient arrangements and successfully reproduced the experimental results. Therefore, we conclude that the additional Sn state originates from Sn atoms neighboring the Sr deficiency. The contents in this chapter is based on Ref. [2].

5.1 Sample characterization

We show PXRD patterns of our samples in Fig. 5.1(a). The NS ($x \simeq 0$) sample exhibits no detectable impurity peaks. All the peaks were indexed with the space group $Pm\bar{3}m$ (No. 221, O_h^1) and a lattice parameter of $a = 0.5138$ nm of Sr_3SnO [44]. For the pattern of the D ($x \simeq 0.5$) sample, the peaks were indexed with $a = 0.5125$ nm except for the left shoulder peaks originating from insulating SrO, which also has a cubic crystalline structure (space group No. 225, $Fm\bar{3}m$, O_h^5) with a slightly larger lattice parameter $a = 0.5146$ nm. Figure 5.1(b) shows the temperature dependence of the magnetizations of these samples. The NS sample does not show superconductivity of $Sr_{3-x}SnO$. As shown in the inset, the magnetization very slightly decreases below 3.7 K, which originates from the su-

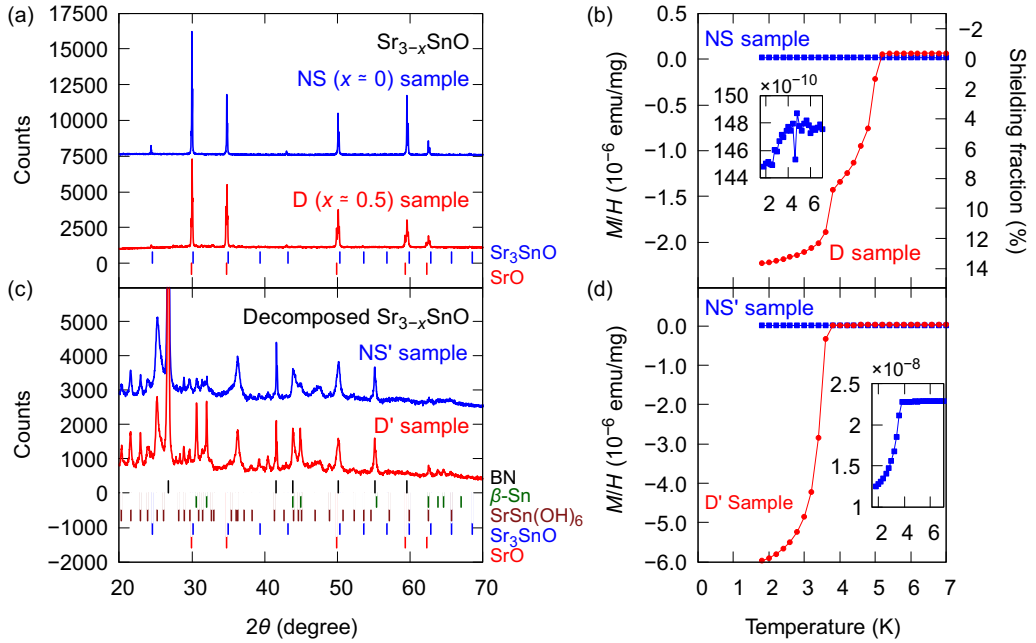

Fig. 5.1 (a) Powder x-ray diffraction patterns of the nearly stoichiometric (NS) sample (prepared with the Sr-excess condition of $x_0 = -0.5$) and Sr-deficient (D) sample (prepared with the Sr-deficient condition of $x_0 = +0.5$). The bars at the bottom indicate the peak positions of Sr_3SnO (PDF 01-084-0254) and SrO (PDF 01-075-6979). (b) Temperature dependence of the magnetization of $Sr_{3-x}SnO$ measured in a magnetic field of $\mu_0 H = 1$ mT under a zero-field-cooling (ZFC) condition. The inset show a magnified view for the NS sample. (c) X-ray diffraction patterns after the NS and D samples were intensionally decomposed in air (NS' and D' samples, respectively). The bars at the bottom indicate the peak positions of BN (PDF 00-034-0421), β-Sn (PDF 01-086-2265), $SrSn(OH)_6$ (PDF 00-009-0086), Sr_3SnO, and SrO. (d) Temperature dependence of the magnetization of the NS' and D' samples measured in a magnetic field of $\mu_0 H = 2$ mT and under a ZFC condition. The inset shows a magnified view for the NS' sample. When evaluating magnetization, the mass of the mixed BN and polyethylene powder was subtracted.

perconductivity of tin impurity that was not detected with PXRD. In contrast, the D sample shows the Meissner effect below 5 K, originating from the superconductivity of $Sr_{3-x}SnO$ [7]. The shoulder-like structure at 3.7 K is attributable to the superconductivity of Sn impurity. Comparing magnetization data above and below 3.7 K, we estimate the diamagnetism due to superconductivity of β-Sn as 0.58×10^{-6} emu/mg, which corresponds to 5.4 weight percent or 14 mole percent of β-Sn inclusion.

After the magnetization and Mössbauer measurements, both NS ($x \simeq 0$) and D ($x \simeq 0.5$) samples were intentionally decomposed in air for a few days [hereafter referred to as NS' and D' samples] and their PXRD patterns and magnetizations were measured again. The large peak at $2\theta = 27°$ as well as several others in the PXRD pattern [Fig. 5.1(c)] originate from boron nitride mixed for the Mössbauer experiments. The decomposed samples mainly consist of $SrSn(OH)_6$. In addition, the D' sample exhibits clear peaks from β-Sn whereas the peaks from β-Sn in the NS' sample are rather faint. As shown in Fig. 5.1(d), the D' sample exhibits strong diamagnetism below 3.7 K due to the superconductivity of Sn. The NS' sample also exhibits much weaker diamagnetism as shown in the inset.

5.2 Mössbauer spectra

^{119}Sn-Mössbauer spectra of $Sr_{3-x}SnO$ samples at various temperatures are presented in Fig. 5.2. Both NS ($x \simeq 0$) and D ($x \simeq 0.5$) samples strongly absorb the γ ray around the isomer shift of +1.9 mm/s. This shift is very close to that of Mg_2Sn (+1.87 mm/s at 300 K [59]), in which the Sn^{4-} state is anticipated. In addition, minor γ-ray absorptions are observed at slightly higher isomer shifts, as evidenced by the shoulder-like structure in the spectra.

To analyze the data more quantitatively, we fitted the spectra with multiple Lorentzian functions and evaluated their isomer shifts and integrated peak intensities. For the NS sample, we used two Lorentzians to fit the major and minor absorptions [Fig. 5.2(c)]. We confirmed that the minor absorption is not due to β-Sn impurity because the observed isomer shift of +3.03(2) mm/s at the lowest temperature is clearly different from the reported isomer shift of β-Sn (2.60 mm/s at 4.2 K [77]). For the D sample, we added one extra Lorentzian to take into account the contribution of the β-Sn impurity [Fig. 5.2(d)]. The isomer shift of the Sn impurity is fixed to the reported value. The intensity is also fixed so that the integrated peak area becomes 14% of the total area at the lowest temperature as calculated from the temperature dependence of the magnetization [Fig. 5.1(b)]. The fitting well explains the data, and the isomer shift of the minor absorption at 3 K was evaluated to be +2.973(11) mm/s, which is again distinct from the isomer shift of β-Sn. Thus, this minor absorption of the D sample should be intrinsic to $Sr_{3-x}SnO$.

From the integrated intensity of the spectra at the lowest temperature, the fractions of the tin atoms related to these minor absorptions are estimated to be 16.4(9)% in the NS ($x \simeq 0$) sample and 27.9(12)% in the D ($x \simeq 0.5$) sample. Since the intensity of the minor absorption increases with the strontium deficiency, the tin atoms near the Sr deficiency are ascribable to the origin of this minor absorption.

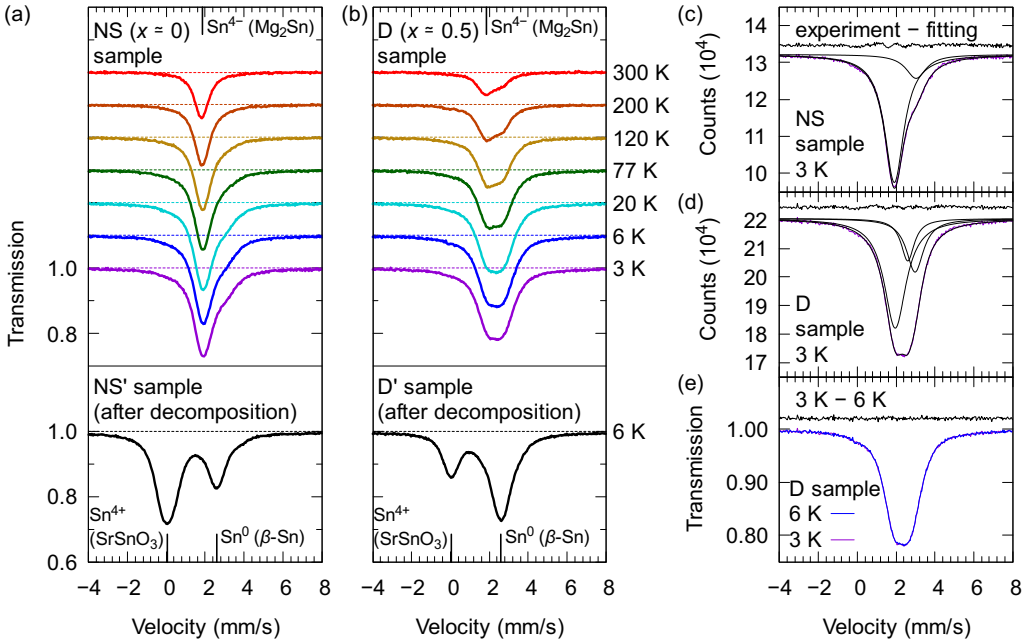

Fig. 5.2 Temperature dependence of the ^{119}Sn-Mössbauer spectra of (a) the nearly stoichiometric (NS) and (b) Sr-deficient (D) $Sr_{3-x}SnO$ samples. All spectra have the same scale, and each spectrum is shifted upward by 0.1 so that the change of the peak shape is more visible. The dashed line for each spectrum indicates the transmission of 100%. For each panel, the bottom spectrum was obtained at 6 K after intensional decomposition in air (NS' and D' samples). The vertical lines at 1.87 mm/s, 0.05 mm/s, and 2.60 mm/s indicate the isomer shifts of Mg_2Sn at 300 K [59], $SrSnO_3$ at 100 K [76], and β-Sn at 4.2 K [77], respectively, representing Sn^{4-}, Sn^{4+}, and Sn^0 ionic states. (c, d) Results of Lorentzian fittings of the spectra of the NS and D samples at 3 K for quantitative analysis of the isomer shifts and absorption intensities. The sum of the Lorentzians reasonably reproduces the experimental spectra. (e) Comparison of the spectra above (6 K, blue curve) and below (3 K, purple curve) the superconducting transition temperature of the D sample. The two spectra almost overlap each other, and the difference between the two spectra (shifted upward) is a straight line within the noise level.

In order to estimate the amount of the Sr deficiency x, let us assume for simplicity that the $Z = 12$ Sr atoms surrounding a Sn atom can be extracted independently. In this case, the probability that a Sn atom does not have any neighboring Sr deficiency is $(1 - x/3)^Z$. Then, the relative intensity of the minor absorption, originating from Sn atoms next to Sr deficiencies, is given by $1-(1-x/3)^Z$. Assuming that the observed 16% minor absorption in the NS ($x \simeq 0$) sample is explained

by this formula, we obtain $x = 0.04$. This estimated value of x is consistent with the results of EDX, yielding $x = 0.02$ as explained above. This good agreement confirms the scenario that minute spontaneous Sr deficiency leads to a minor absorption with relatively strong intensity. Similar amount of the Ca deficiency is reported by EPMA in a single crystal of Ca_3PbO [45]. Such amount of deficiency should be insufficient to trigger superconductivity. For the D ($x \simeq 0.5$) sample, the same assumption leads to the equation $1 - (1 - x/3)^Z = 0.28$, whose solution is $x \simeq 0.08$. This value is substantially smaller than the nominal Sr deficiency of $x_0 = 0.5$, probably because the simple assumption of independent deficiency distribution is no longer valid for such a large value of x. This implies that the Sr deficiencies tend to cluster each other, rather than distributing just randomly, when the amount of deficiency becomes larger.

Let us discuss the origin of the minor absorption in more detail. As explained in Chapter 3, p or d electrons result in a negative and smaller shift for the Sn nucleus. Therefore, it is expected that the minor absorption with a larger isomer shift originates from tin ions with less p electrons than Sn^{4-}; or in other words, the hole-doped ionic states due to strontium deficiency.

In order to confirm that the minor absorptions do not originate from partial decomposition of the samples, we measured Mössbauer spectra of the intentionally decomposed samples [NS' and D' samples]. After the decomposition, the γ-ray absorptions are located at 0.0–0.1 mm/s and 2.6 mm/s at 6 K. These absorptions are very similar to those of $SrSnO_3$ (0.05 mm/s at 100 K [76]) and β-Sn (2.60 mm/s at 4.2 K [77]). This result indicates that $Sr_{3-x}SnO$ decomposes into β-Sn and a certain material containing Sn^{4+} ion [presumably $SrSn(OH)_6$ as seen in the PXRD pattern], and possibly some other compounds without tin. If the samples had decomposed during the setup of the Mössbauer experiments, we would have observed the absorption of Sn^{4+}. However, the actual spectra of the pristine samples do not show any absorption at around 0 mm/s. Therefore, we can exclude the possibility that the minor absorptions originate from partial decomposition.

To examine the temperature evolution of the Mössbauer effect, we plot the temperature dependence of the isomer shift and integrated intensity in Fig. 5.3. The isomer shifts of the major absorptions are almost equal in the NS ($x \simeq 0$) and D ($x \simeq 0.5$) samples. This fact suggests that the strontium deficiency affects so locally to the density of electrons at the nucleus position that a major fraction of the tin atoms remains unchanged from Sn^{4-} even in the D sample.

From the temperature dependence of the integrated intensity plotted in Fig. 5.3(b), we can calculate the energy of the local vibration of a Sn atom. Assuming that the intensity is proportional to the recoil-free fraction f, the data was fitted with the Debye model [60]. As shown in Fig. 5.3(b), the fitting reproduces well the temperature dependences of all absorptions. The extracted

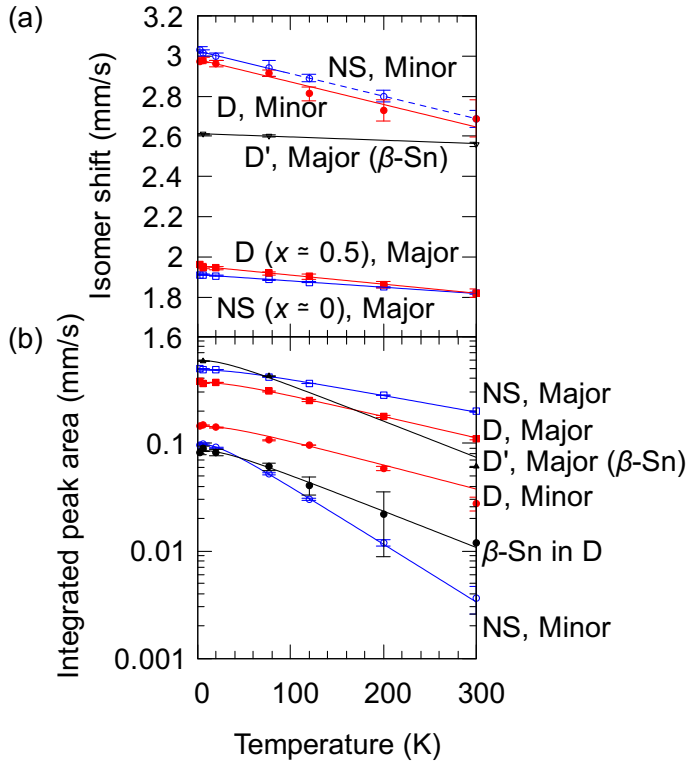

Fig. 5.3 Temperature dependence of (a) the isomer shifts and (b) integrated peak areas obtained by fitting the spectra with multiple Lorentzians. For the contribution from the β-Sn impurity in the D ($x \simeq 0.5$) sample, we assumed that the integrated peak area exhibits the same temperature dependence as that of β-Sn contained in the D' sample. For the NS ($x \simeq 0$) sample and at temperatures above 100 K, the double-Lorentzian fitting with six independent parameters (two sets of the peak position, intensity, and width) was not successful because of the too small contribution from the minor absorption. We estimated the isomer shift of the minor absorption by the following way and fixed the shift in the fitting (i.e. now we used five independent parameters). First, we assumed that the isomer shift of the minor absorption exhibits a linear temperature dependence. Then the slope of the temperature dependence is assumed to be the same as that of the D sample. Under these assumptions, we extrapolated the data of the NS sample below 100 K to higher temperatures to estimate the isomer shift at 120 K, 200 K, and 300 K, as indicated with the blue broken line in the panel (a).

Table 5.1 Isomer shifts (IS) at 300 K and effective Debye temperatures (Θ_D) characterizing the vibration of the Sn atoms, obtained from experiments and calculations. The accuracy of the experimental isomer shifts is expected to be about 0.01 mm/s. The error of the experimental values are defined as the standard error of double-Lorentzian fitting. As for the major absorption of the NS ($x \simeq 0$) sample, the standard error of the fitting is smaller than the expected accuracy. The accuracy of the calculated isomer shifts is around 0.2 mm/s.

Absorption	IS (mm/s)	Θ_D (K)
Major [NS ($x \simeq 0$) sample]	1.82	222(3)
Major [D ($x \simeq 0.5$) sample]	1.82(2)	196(2)
Sr_3SnO (calculation)	1.7	186.5(8)
Sn1 in "$Sr_5Sn_2O_2$" (calculation)	1.9	
Minor (NS sample)	2.69(4)[a]	119.8(6)
Minor (D sample)	2.69(9)	185(7)
β-Sn in the D' sample	2.56(1)	151(8)
"$Sr_2Sn_2O_2$" (calculation)	3.1	97(3)
"$Sr_3Sn_2O_2$" (calculation)	2.8	148.5(18)
"$Sr_4Sn_2O_2$" (calculation)	2.4	148.3(13)
Sn2 in "$Sr_5Sn_2O_2$" (calculation)	2.4	

[a] Evaluated by linear extrapolation from the data at low temperatures (not by the Lorentzian fitting): extrapolation error is presented.

Θ_D, as well as the isomer shifts, are summarized in Table 5.1. Comparing Θ_D of all absorptions, there is a tendency that Θ_D decreases as the isomer shift increases. This tendency can be again understood as the effect of the local strontium deficiency: the higher local strontium deficiency corresponds to the lower density of the p electrons at the tin atoms and weaker binding of the atoms to the lattice.

We also tried fitting with the Einstein model [60]:

$$\langle r^2 \rangle_E = \frac{\hbar^2}{2Mk_B\Theta_E} \coth\left(\frac{\Theta_E}{2T}\right), \tag{5.1}$$

where Θ_E is the effective Einstein temperature. The fitting is as good as that with the Debye model but has slightly larger residual sum of squares. We found that $\sqrt{3}\Theta_E$ gave almost the same temperature as Θ_D. This agrees with the theoretical relation $\sqrt{3}\Theta_E = \Theta_D$ deduced under the assumption of the same mean square displacements in the Einstein and Debye solids at high temperature: $\langle r^2 \rangle_E = \langle r^2 \rangle_D$ [60].

Before closing this subsection, we would like to comment on the Mössbauer spectrum in the superconducting state. We did not observe any clear difference in the spectra across the superconducting transition as shown in Fig. 5.2(e). Since superconductivity does not cause large change in the electronic density at the nucleus, the superconducting transition is in most cases difficult to be observed with Mössbauer spectroscopy in terms of the isomer shift [78] and the recoil-free fraction [79]. To observe superconductivity in $Sr_{3-x}SnO$ in the Mössbauer spectroscopy, we need to enhance the resolution as well as to use samples with a larger superconducting volume fraction. These are the focus of future works.

5.3 First-principles calculations

The relation between the experimental isomer shift (IS) at room temperature [59, 72] and calculated electronic density at the Sn-nucleus position for various compounds are summarized in Fig. 5.4. We find an anticipated linear relation [58]: $\mathrm{IS} = \alpha\,\Delta\rho + \beta$ with $\alpha = 0.071(2) a_\mathrm{B}^3$ mm/s and $\beta = -0.03(6)$ mm/s, where $\Delta\rho$ is the electronic density with respect to that of $BaSnO_3$ (262122.8 a_B^{-3} in our calculation). The coefficient α is smaller than the previously reported values by 10–20% [80, 81]. This discrepancy should originate from the difference in the calculation methods.

From this relation, the isomer shift can be estimated from the electron-density calculation with the accuracy of around 0.2 mm/s. The calculated isomer shifts of $Sr_{3-x}SnO$ are listed in Table 5.1. The isomer shift of the major absorption agrees with the calculation for Sr_3SnO. For the minor absorption, we calculated the density of electrons assuming various hypothetical arrangements of the Sr deficiency and found that the calculated isomer shift of "$Sr_3Sn_2O_2$" [Fig. 3.4(c)] reasonably reproduces the observed values of the minor absorptions.

We also calculated the electronic density for "$Sr_5Sn_2O_2$" shown in Fig. 3.3(b). This unit cell contains two distinct Sn sites: Sn1 neighboring no Sr deficiencies and Sn2 neighboring four deficiencies. The calculation revealed that the isomer shift of Sn1 is almost unchanged from that of Sr_3SnO and that the isomer shift of Sn2 is the same as "$Sr_4Sn_2O_2$," whose Sn site is also neighboring four Sr deficiencies. Thus, even if two Sn sites with and without neighboring Sr deficiency are next to each other in a single phase, the γ-ray absorption splits into two instead of shifting continuously.

The force constant k of the Sn atom in $Sr_{3-x}SnO$ was estimated from the change in the total energy due to a virtual displacement of the Sn atom towards the nearest neighboring strontium atom (See the arrows in Fig. 3.4): $\Delta E = k(r - r_0)^2/2 + E_0$, where ΔE is the change in energy, r is the displacement of the Sn atom, r_0 is the stable atomic position along the direction of displacement, and E_0 is

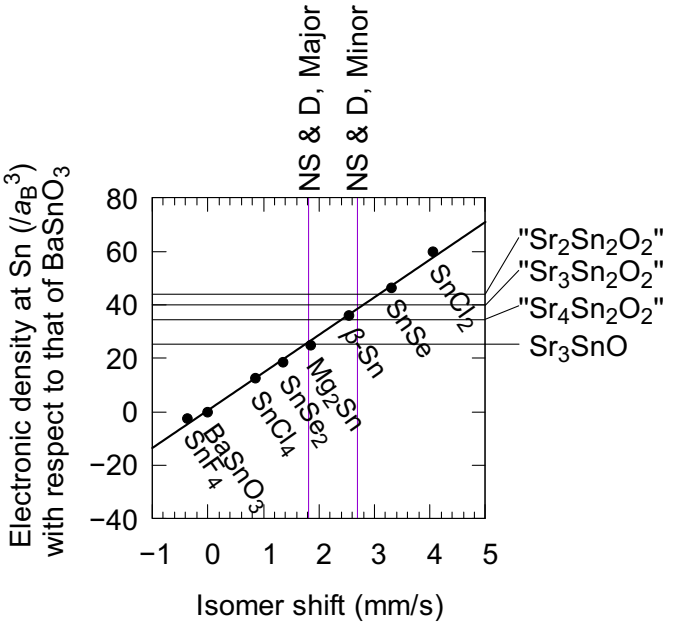

Fig. 5.4 Calculated electronic density versus experimental isomer shifts at room temperature [59, 72]. The thick solid line shows the result of the linear fitting to the data points. The thin horizontal and vertical lines indicate the calculated electronic densities at the Sn nucleus of various Sr_3SnO-based structures and observed isomer shifts of the NS ($x \simeq 0$) and D ($x \simeq 0.5$) samples, respectively.

the minimum energy corresponding to $r = r_0$. The effective Debye temperature was then calculated by $\Theta_D = \sqrt{3}\Theta_E = \sqrt{3}\,(\hbar/k_B)\sqrt{k/M}$ [60]. Figure 5.5 shows the change in energy and results of the fitting. The extracted effective Debye temperatures are listed in Table 5.1. The overall trend of the decreasing Θ_D with the increase of the isomer shift is reproduced in calculation. The calculated Θ_D of Sr_3SnO and the experimental Θ_D of the major absorption of the NS ($x \simeq 0$) sample differs by 16%. For the minor absorptions, the calculated Θ_D of "$Sr_2Sn_2O_2$" and "$Sr_3Sn_2O_2$" matches by similar accuracy with the experimental Θ_D of the minor absorptions in the NS and D ($x \simeq 0.5$) samples, respectively.

These good agreements between the calculated and experimental values confirms that the origins of the major and minor absorptions are the tin atoms without and with the neighboring strontium deficiency, respectively. We note that the local deficiency is more in the NS ($x \simeq 0$) sample than in the D ($x \simeq 0.5$) sample based on the estimation of Θ_D of the minor absorptions. This may be due to the slow cooling in the end of the synthesis of the NS sample; the stoichiometric Sr_3SnO solidifies first and $Sr_{3-x}SnO$ with a large deficiency is formed later as a minority

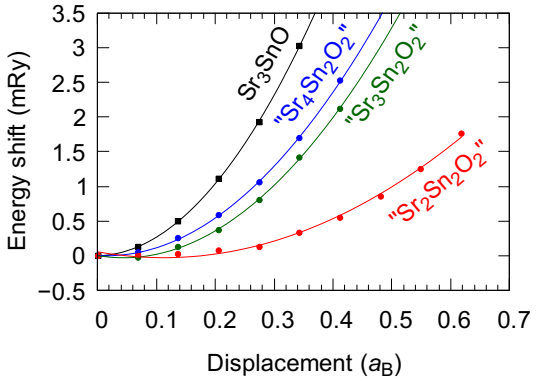

Fig. 5.5 Total energies of Sr_3SnO, "$Sr_4Sn_2O_2$," "$Sr_3Sn_2O_2$," and "$Sr_2Sn_2O_2$" as functions of the displacement of the Sn atom calculated using the WIEN2k program. More Sr-deficient structures exhibit smaller changes in the total energy with displacement of the Sn atom, meaning that these materials have lower force constants of the lattice. In the highly deficient structures, the relative energy once goes negative with a small displacement. This means that the original atomic position (zero displacement) is unstable. Therefore, we fitted the data with the function $\Delta E = k(r - r_0)^2/2 + E_0$ with the stable atomic position r_0, the force constant k, and the minimum energy E_0 as fitting parameters.

phase. In the case of the D sample, in contrast, relatively rapid cooling leads to a large amount of deficient $Sr_{3-x}SnO$ but with relatively dilute deficiency.

5.4 Comparison with NMR

We comment that the phase splitting into the nearly stoichiometric and deficient compounds has been suggested in the previous study of magnetization [9] and indeed observed with NMR [50]. Since NMR probes properties of the conduction electrons though it measures the Zeeman energy of the Sn nucleus, the splitting in the NMR spectrum suggests that one sample consists of two materials ("phases") with distinct stoichiometries as shown in Fig. 5.6. Similar phase splitting must exist also in the current samples, judging from the shielding fraction lower than 100%. On the other hand, the Mössbauer spectroscopy detects the local information at the nucleus position, and thus the two absorptions may originate from two sites in each phase. Since highly deficient phases such as "$Sr_3Sn_2O_2$" and "$Sr_2Sn_2O_2$" will be chemically unstable, it is unlikely that one sample separates into the two phases Sr_3SnO and "$Sr_3Sn_2O_2$." Thus, we conclude that the mi-

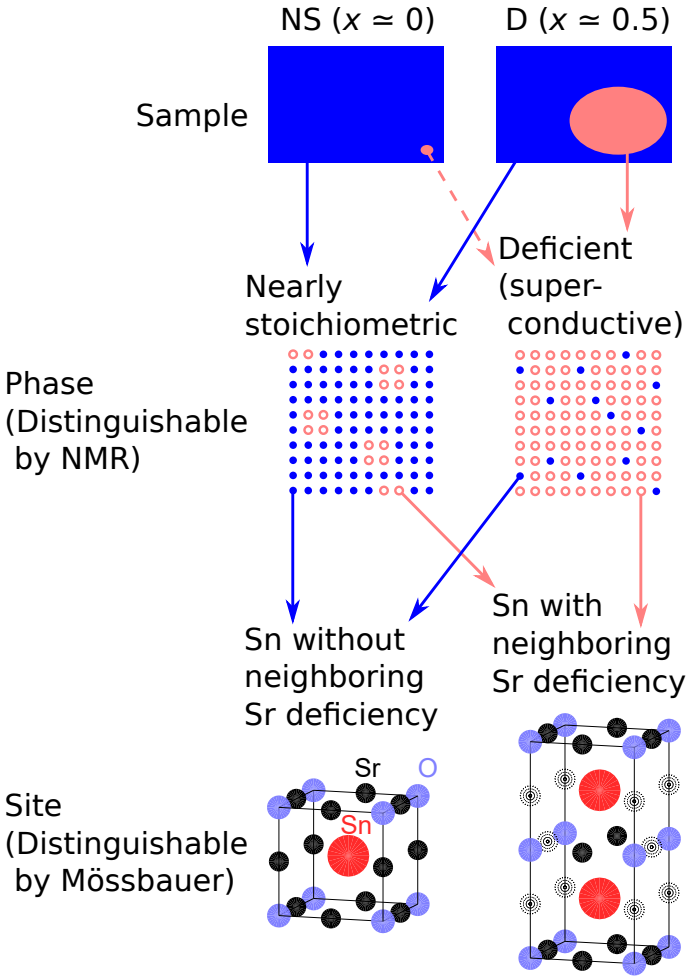

Fig. 5.6 Schematic illustration of the phase and site splittings. The NS sample is dominated by the nearly stoichiometric phase (blue) possibly with a separated inclusion of the deficient phase (red). In contrast, the D sample contains about 10% of the deficient superconductive phase. The nearly stoichiometric phase consists mostly of the Sn atom without the neighboring deficiency of Sr (blue solid circles) while the superconductive phase is composed mainly of the Sn atom with neighboring deficiency (red open circles).

nor absorption reflects the local Sr deficiency in each of the phases contained in $Sr_{3-x}SnO$ with $x \simeq 0$ in the NS sample and with $x \simeq 0.5$ in the D sample.

To sum up, we consider that our samples contain nearly stoichiometric and deficient phases as depicted in Fig. 5.6. Each of these phases contains Sn sites with and without neighboring Sr deficiencies. Previous NMR measurements observed the phase splitting but could not detect such site splitting within each phase. In

contrast, the Mössbauer spectroscopy detects the difference in the Sn sites with and without neighboring Sr deficiency but hardly distinguishes similar sites in different phases.

The present results confirm the Sn^{4-} state and thus the validity of the band structure calculations. In this sense, these results are consistent with the NMR experiments observing the $1/T_1$ attributable to the Dirac dispersion [50]. Furthermore, since the large amount of the Sr deficiency to "$Sr_3Sn_2O_2$" or "$Sr_2Sn_2O_2$" leads to heavy hole doping, the deficient phase with a large portion of such Sn sites with neighboring Sr deficiency would exhibit metallic $1/T_1$, as indeed observed in the NMR measurements.

5.5 Conclusion of this chapter

By combining the Mössbauer spectroscopy and first-principles calculations, we confirmed the Sn^{4-} state in the antiperovskite oxide $Sr_{3-x}SnO$. Furthermore, we identified the origin of the minor absorption to be the Sn atoms with the neighboring Sr deficiency. These results support the idea that $Sr_{3-x}SnO$ is a doped Dirac superconductor.

Chapter 6

Possible unconventional superconductivity in $Sr_{3-x}SnO$ investigated by μSR

In this chapter, we report μSR results of $Sr_{3-x}SnO$. We observed a clear increase of the transverse-field muon spin depolarization rate $\sigma_{\rm tf}$ below $T_{\rm c}$. This result provides a definite evidence of the bulk superconductivity in this material. $\sigma_{\rm tf}$ exhibits exponential behavior at low temperatures, indicating the absence of nodes in the superconducting gap. The deduced London penetration depth for $T \to 0$ is 320–1020 nm and the ratio $T_{\rm c}/\lambda(0)^{-2}$ is comparable to those of high-temperature superconductors. This fact possibly indicates an unconventional pairing mechanism. We also performed μSR under zero field and did not detect breaking of the time-reversal symmetry. These results do not exclude the possibility of the theoretically suggested unconventional superconductivity belonging to the same symmetry as the Balian-Werthamer (BW) state [82], as well as the possibility of the ordinary s-wave superconductivity [8]. The contents in this chapter is based on Ref. [3].

6.1 Magnetic susceptibility and specific heat

First, we show the DC magnetic susceptibility of the $Sr_{3-x}SnO$ samples in Fig. 6.1. All samples exhibit superconductivity at around 5.4 K. We call this primary superconducting phase the 5-K phase. The kink at 3.7 K is attributable to the superconductivity of Sn impurity, which was barely seen in PXRD patterns. For Sample A, the superconducting volume fraction evaluated from the DC susceptibility without the demagnetization correction reaches 11% at 1.8 K. In the case of Sample B, the volume fraction is 9% under 5 mT and the fraction decreases with

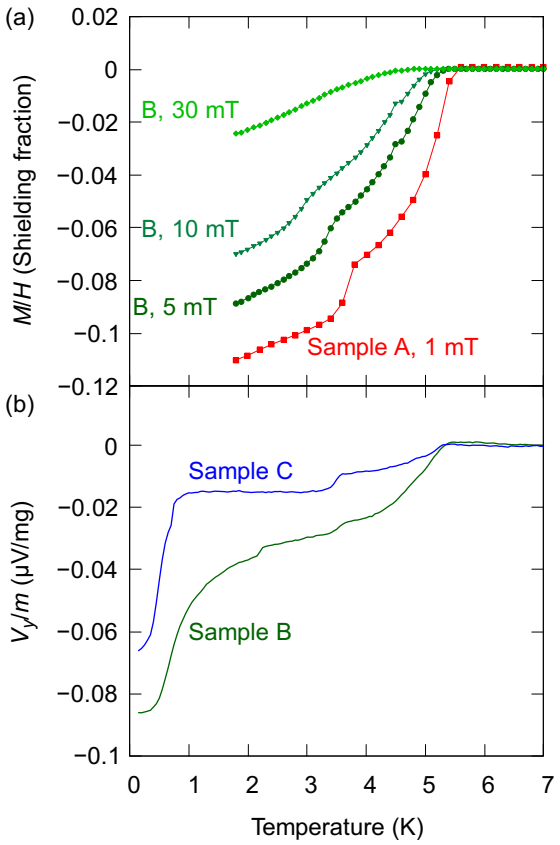

Fig. 6.1 (a) DC magnetic susceptibility of Sample A measured under 1 mT and that of Sample B under 5, 10, and 30 mT. Both samples exhibit strong diamagnetism below $T_c \simeq 5.4$ K of $Sr_{3-x}SnO$ with the shielding fractions of around 10% at 2 K. The kink at 3.7 K originates from superconductivity of Sn impurity. (b) Voltage signal detected with a mutual inductance coil normalized by the sample mass (corresponding to the real part of the AC susceptibility) of Samples B and C. For both sets of data, the measurements were performed under an AC field with the amplitude of 16 μT and the frequency of 3011 Hz. Both samples exhibit superconducting transition at $T_c \simeq 5.3$ K and 0.8 K. Sample C exhibits a weaker 5-K transition but a sharper 0.8-K transition than Sample B.

increasing the field. Considering that the fields applied during the measurements of Sample B are stronger, we expect that the superconducting volume fraction of the 5-K phase is almost the same in both samples. The volume fraction smaller than 100% is attributable to the phase separation into multiple compositions with different amount of Sr deficiency [9, 50]. The onset of the transition decreases to 4.9 K under 30 mT. Figure 6.1(b) shows the AC susceptibility down to 0.2 K of Samples B and C measured under zero DC field. Both samples exhibit additional superconducting transition at around 0.8 K as reported [7]. We hereafter call this second superconducting phase the 0.8-K phase. The origin of the 0.8-K phase is not clear yet, but the separation into two phases with slightly different amount of the Sr deficiency may cause such splitting of the transitions [9]. From these results, we infer that Sample B contains more 5-K phase than the 0.8-K phase, whereas Sample C contains more 0.8-K phase. Sample D has a diamagnetic ratio between 5-K and 0.8-K phases similar to Sample C, or Sample D is dominated by the 0.8-K phase. Thus, comparing the μSR results of these samples, we may unveil the difference in the superconducting properties of the 5-K and 0.8-K phases.

Next, we present in Fig. 6.2 the electronic specific heat C_e divided by temperature T of Sample D at low temperature. We observed a clear anomaly at around 0.85 K. We fitted the temperature dependence using the Bardeen-Cooper-Schrieffer (BCS) theory [83] and the phononic contribution, which is already subtracted in Fig. 6.2. We fixed $T_c = 0.85$ K to satisfy the entropy balance. We obtained the Sommerfeld coefficient $\gamma = 5.67(3)$ mJ mol^{-1}K^{-1}, the Debye temperature $\Theta_D = 119.9(2)$ K, and the volume fraction of 23%. This fact evidences the bulk nature of the 0.8 K phase.

6.2 μSR under 30 mT

Figure 6.3 compares the μSR time spectra, recorded above and below T_c, measured under an applied field of 30 mT for Sample A. The presence of the randomly oriented nuclear moments causes a weak relaxation of the μSR signal above T_c. The relaxation rate is enhanced below T_c, which is caused by the formation of a flux-line lattice in the superconducting state, giving rise to an inhomogeneous magnetic field distribution. By fitting the data with the Gaussian cosine function, we found that σ changes from 0.084(6) μs^{-1} at 7 K to 0.160(4) μs^{-1} at 1.6 K. This change in σ is readily seen in the raw data, namely the faster damping at 1.6 K. The change in the relaxation rate across T_c indicates that a large portion of the muons stopped at the superconducting region of the sample.

We measured σ as a function of the applied field at 1.5 K and 3.5 K (see Fig. 6.4). Each point was obtained by field cooling the sample from above T_c to 1.7 K. First, σ strongly increases with increasing magnetic field until reaching a

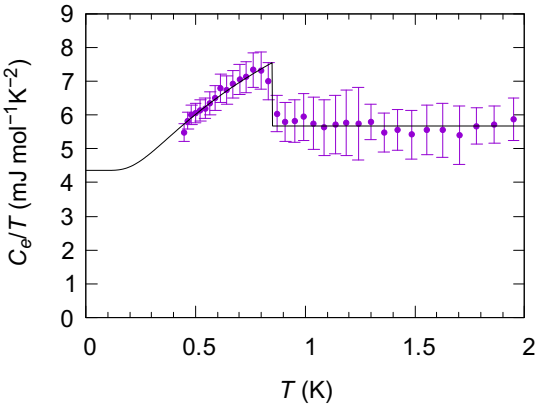

Fig. 6.2 Electronic specific heat divided by temperature C_e/T. We observed a clear superconducting transition at 0.85 K with a volume fraction of 23%, evidencing the bulk superconductivity. The solid curve represent the fitting with the BCS theory.

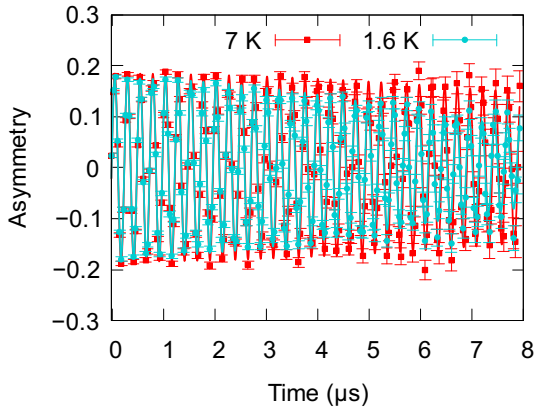

Fig. 6.3 Transverse-field μSR spectra for Sample A under 30 mT at 7 K (red squares) and 1.6 K (blue circles). The oscillation of the asymmetry decays faster at 1.6 K than at 7 K due to the spatial distribution of the local magnetic field caused by flux-lattice formation. The solid curves are results of the fittings with the Gaussian cosine function.

maximum at 15 mT and then above it continuously decreases up to the highest field (100 mT) investigated. The observed field dependence of σ implies that for a reliable determination of the penetration depth, the applied field must be just above the peak. Thus, we measured the temperature dependence of σ at 30 mT.

The temperature dependence of σ for Sample C under an applied field of 30 mT is shown in Fig. 6.5. An increase of σ was observed below $T_c = 6$ K. The relaxation rate is related to the London penetration depth $\lambda(T)$ as Eq. 3.6. Moreover, the temperature dependence of λ for the isotropic as well as anisotropic superconducting gaps can be calculated using the BCS theory:

$$\frac{\lambda^{-2}(T)}{\lambda^{-2}(0)} = 1 + \frac{1}{2\pi}\int\int_0^\infty \frac{\partial f_{\boldsymbol{k}}}{\partial E_{\boldsymbol{k}}} \mathrm{d}\varepsilon \mathrm{d}\hat{\boldsymbol{k}}, \tag{6.1}$$

where $f_{\boldsymbol{k}} = [1 + \exp(E_{\boldsymbol{k}}/(k_B T))]^{-1}$ is the Fermi distribution function, k_B is the Boltzmann constant, $E_{\boldsymbol{k}} = \sqrt{\varepsilon^2 + \Delta_{\boldsymbol{k}}^2(T)}$ is the quasiparticle excitation energy of the superconducting state with the kinetic energy ε relative to the Fermi energy ε_F and the superconducting gap $\Delta_{\boldsymbol{k}}(T) = \Delta_0(T)Y(\hat{\boldsymbol{k}})$ [83]. The temperature dependence of Δ_0 is obtained by solving the gap equation [84]

$$\frac{1}{4\pi}\int\int_0^{\varepsilon_c} \frac{1}{E_{\boldsymbol{k}}} \tanh\left(\frac{E_{\boldsymbol{k}}}{2k_B T}\right) Y^2(\hat{\boldsymbol{k}}) \mathrm{d}\epsilon \mathrm{d}\hat{\boldsymbol{k}} = \text{const.}, \tag{6.2}$$

where ε_c is a cutoff energy. The constant value in the right-hand side is numerically obtained by substituting $T = T_c$ and $\Delta_0 = 0$. We simply set the cutoff energy and the Fermi energy as $\varepsilon_c = 100 k_B T_c$ and $\varepsilon_F = 2000 k_B T_c$. These values are compared to the Debye temperature $\varepsilon_D = 35 k_B T_c$ measured by ^{119}Sn-Mössbauer spectroscopy [2] and $\varepsilon_F = 2000 k_B T_c$ estimated from the band structure calculation [1].

We calculated the temperature dependence of the relaxation rate assuming two superconducting gap structures on a spherical Fermi surface: $Y(\hat{\boldsymbol{k}}) \equiv 1$ for a fully gapped and $Y(\hat{\boldsymbol{k}}) = \sqrt{\hat{k}_x^2 + \hat{k}_y^2}$ for a point-nodal states. While σ saturates at low temperatures for a fully gapped state (the solid curve in Fig. 6.5), σ continues to increase as lowering temperature for a point-nodal state (the dashed curve). Both fitting curves reasonably match the experimental result within the experimental error, but the root mean square error is smaller for the fully gapped state (1.2758) than for the point-nodal state (1.3933). Although it is theoretically suggested that the superconductivities with a full gap and point nodes have similar transition temperatures [8], this fitting analysis suggests that the fully gapped superconductivity such as the ordinary s-wave superconductivity or the topological superconductivity resembling the BW state is more likely to be realized in $Sr_{3-x}SnO$.

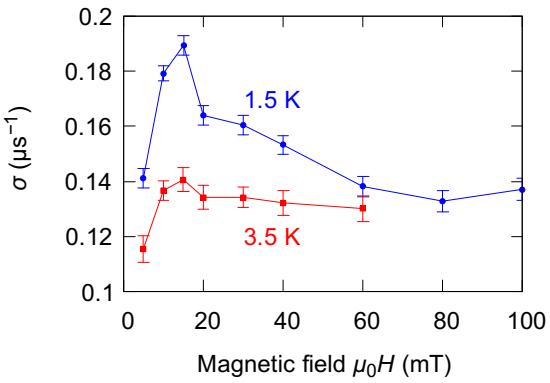

Fig. 6.4 Muon spin depolarization rate σ of Sample A as a function of the applied magnetic field measured at 3.5 K (red squares) and 1.5 K (blue circles). The enhancement of σ below 20 mT and at 1.5 K are attributable to the superconductivity of Sn impurity with $H_c = 30.9$ mT at $T = 0$ K [85].

Figure 6.6 compares $\sigma(T)$ of all samples measured under 30 mT. Assuming a fully gapped superconductivity, the fitting yields $T_c = 6.3(2)$ K and $\lambda(0) = 875(9)$ nm for Sample A, $T_c = 6.2(2)$ K and $\lambda(0) = 1018(11)$ nm for Sample B, and $T_c = 6.2(2)$ K and $\lambda(0) = 878(10)$ nm for Sample C. For all samples, we obtained higher T_c than those in the magnetic measurements in Fig. 6.1, probably because μSR detects the superconducting transition of a small part of the sample with slightly higher T_c. Using the coherence length of $\xi(0) = 27$ nm evaluated from the upper critical field [7], the Ginzburg-Landau parameter κ is estimated to be $\kappa = \lambda(0)/\xi(0) = 32$–$38$, suggesting a strongly type-II superconductivity.

λ^{-2} is related to the superfluid density n_S and effective mass m^* through the equation

$$\lambda^{-2} = \frac{\mu_0 n_S e^2}{m^*} \times \frac{1}{1+\xi/l}, \tag{6.3}$$

where μ_0 is the magnetic permeability in vacuum, e is the elementary charge, and l denotes the mean free path [83]. Since the density of states at the Fermi energy $D(\varepsilon_F)$ is evaluated to be $D(\varepsilon_F) = 1.203(7)$ eV^{-1} per unit cell per spin from γ, the superfluid density is estimated to be $n_S = \Delta_0 \times D(\varepsilon_F) \simeq 1.76 k_B T_c D(\varepsilon_F) = 1.7 \times 10^{25}$ m^{-3}. Therefore, the effective mass is calculated to be $m^* = \mu_0 n_S e^2 \lambda^2/(1+\xi/l) < \mu_0 n_S e^2 \lambda^2 = 0.46 m_e$ for Samples A and C and $0.61 m_e$ for Sample B in the clean limit, where m_e is the rest mass of the electron. If the samples are in the dirty limit, m^* is further reduced.

It has been known that T_c and $\lambda(0)^{-2}$ of various materials exhibit a scaling behavior with the ratio $T_c/\lambda(0)^{-2}$ depending on the class of superconductors, as

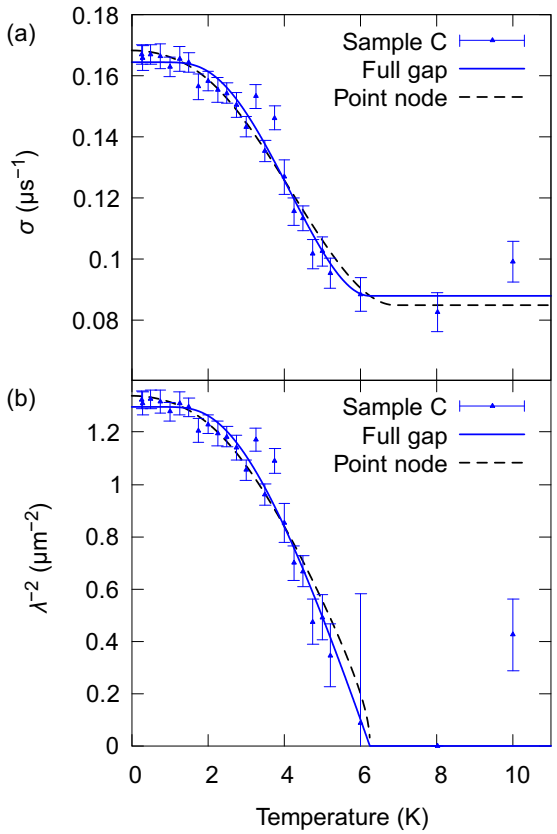

Fig. 6.5 Temperature dependence of (a) the muon spin depolarization rate σ and (b) the penetration depth λ for Sample C under 30 mT. The solid and dashed curves represent fitting results using the theoretical formulae for the fully gapped and point-nodal superconductors, respectively. The fitting curve for the fully gapped state reproduces the experimental results better. Note that the fitting gives a T_c of 6.2 K, somewhat higher than the bulk T_c of 5.4 K.

summarized in the Uemura plot [86, 87]. For some class of superconductors, T_c is very high despite a small n_S. For example, hole-doped cuprate and iron-based superconductors satisfy the relation $T_c/\lambda(0)^{-2} \simeq 4$ K μm^2 [86], whereas element superconductors exhibit much smaller $T_c/\lambda(0)^{-2}$ of less than 0.02 K μm^2 [88]. For the low-carrier superconductors $SrTi_{1-x}Nb_xO_3$ [89] and YPtBi [90], the ratio is $T_c/\lambda(0)^{-2} = 0.267$–$0.496$ and 2.0 K μm^2, respectively. Interestingly, the obtained values of $Sr_{3-x}SnO$ ($T_c = 6$ K and $\lambda(0) = 0.9$–1 μm) give the $T_c/\lambda(0)^{-2}$ ratio close to those of high-temperature or unconventional superconductors as presented in Fig. 6.7: We obtained very large values $T_c/\lambda(0)^{-2} = 4.8$ K μm^2 for Samples A

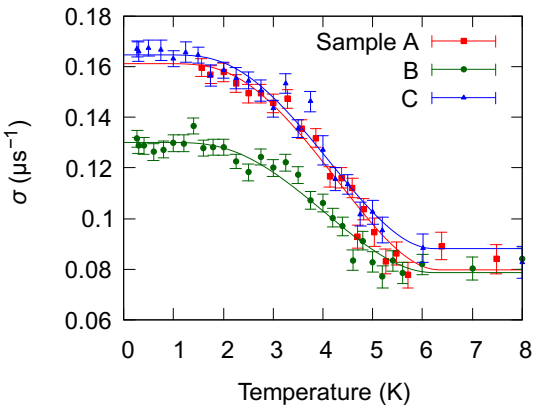

Fig. 6.6 Temperature dependence of the muon spin depolarization rate under 30 mT. The red squares, green circles, and blue triangles are the data for Samples A, B, and C, respectively. The curve on each set of data represents the result of fitting assuming a fully gapped superconducting state.

and C and $T_c/\lambda(0)^{-2} = 6.4\ \mathrm{K}\,\mu\mathrm{m}^2$ for Sample B. These values are between those of the high-temperature superconductors and of the topological superconductor Cu-intercalated Bi_2Se_3, for which $T_c/\lambda(0)^{-2} = 10\ \mathrm{K}\,\mu\mathrm{m}^2$ has been reported [91]. The relatively high T_c for a small number of carriers implies an unconventional superconducting mechanism in $Sr_{3-x}SnO$.

We also performed analyses to take into account the volume fraction of the superconductivity. To do this, we fitted the time-dependent asymmetry of Sample C with two Gaussian cosine functions

$$A\left[\alpha\exp\left(-\frac{\sigma^2t^2}{2}\right)+\exp\left(-\frac{\sigma_N^2t^2}{2}\right)\right]\cos\left(2\pi\gamma_\mu B_0t+\phi\right), \tag{6.4}$$

where σ_N and ϕ are fixed to the values above 6 K and α is fixed to 0.1 for Samples A and B and to 0.04 for Sample C corresponding to the volume fraction of 10 and 4% estimated from the susceptibility measurement in Fig. 6.1, respectively. We obtained $\lambda = 316(23)$ nm, $T_c = 5.6(3)$ K, $T_c/\lambda^{-2} = 0.56\ \mathrm{K}\,\mu\mathrm{m}^2$, and $m^* = 0.053m_e$ for Sample A, $\lambda = 340(11)$ nm, $T_c = 6.05(7)$ K, $T_c/\lambda^{-2} = 0.70\ \mathrm{K}\,\mu\mathrm{m}^2$, and $m^* = 0.067m_e$ for Sample B, and $\lambda = 322(15)$ nm, $T_c = 6.04(5)$ K, $T_c/\lambda^{-2} = 0.62\ \mathrm{K}\,\mu\mathrm{m}^2$, and $m^* = 0.060m_e$ for Sample C. The T_c/λ^{-2} ratios are comparable to those of the low-carrier superconductors. Thus, the qualitative conclusion is still valid even if the phase separation is taken into account.

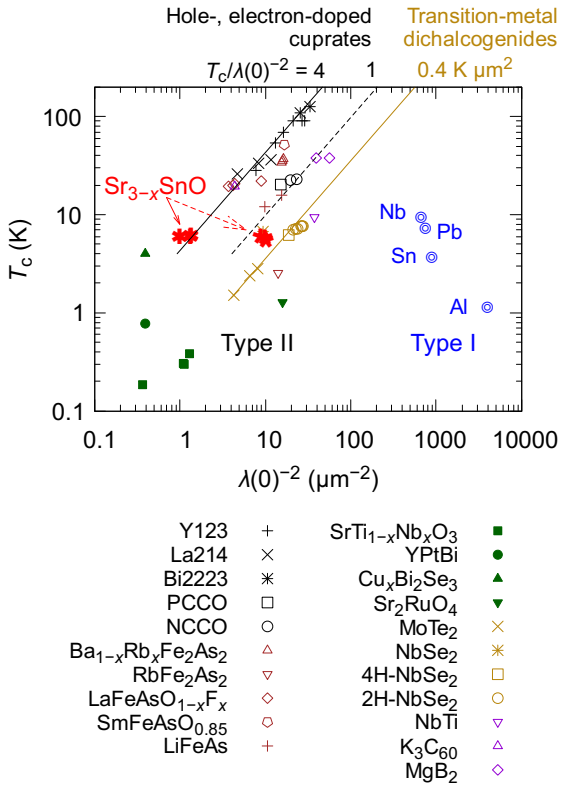

Fig. 6.7 Plot of T_c vs $\lambda(0)^{-2}$ (Uemura plot) for cuprate (black) [92], iron pnictide (brown) [93–97], low-carrier or unconventional (green) [89–91, 98], transition-metal-dichalcogenide (orange) [99–101] elemental s-wave (blue) [88], and compound isotropic (purple) [102–105] superconductors. The solid and dashed lines represent the relations for the hole- and electron-doped cuprates and the transition metal dichalcogenides, namely $T_c/\lambda(0) = 4$, 1, and 0.4 K μm^2, respectively [86, 106]. The large six- and five-spoked asterisks represent the data for $Sr_{3-x}SnO$ obtained from analyses with single and double Gaussian cosine functions, respectively.

6.3 μSR under 5 and 0 mT

Figure 6.8 shows the relaxation rate of Sample C under 5 mT. The jump at 3.0 K probably originates from the superconductivity of Sn. We did not detect the increase of the relaxation rate at 0.8 K, probably because the field modulation caused by the 0.8-K phase is too small under 5 mT even though the superconductivity originates from the bulk. The penetration depth of the 5.4-K phase under 5 mT is calculated to be $8.9(2) \times 10^{-7}$ m. This value is consistent with the one

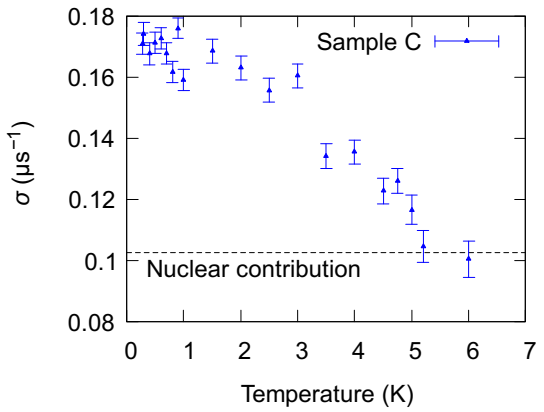

Fig. 6.8 Temperature-dependent relaxation rate of Sample C under 5 mT. The large increase at 3 K probably originates from the superconductivity of Sn impurity.

under 30 mT within the error. Since the magnetic field of 20 mT is reported to completely suppress the 0.8-K phase [9], the upper critical field of the 0.8-K phase may not be large enough for μSR. Measurement of the field dependence of the relaxation rate below 0.8 K remains as a technical challenge in a future work.

Finally, we present in Fig. 6.9 the time dependence of the asymmetry under zero field to test a possible spontaneous time-reversal-symmetry breaking. The data were fitted with the exponential function $A\exp(-\Lambda t)$, and we obtained Λ to be 62(3) ms^{-1} at 6 K, 58(3) ms^{-1} at 1.5 K, and 63(2) ms^{-1} at 0.27 K. Thus, temperature dependence of Λ is quite weak, as shown in the inset of Fig. 6.9. The possible maximum spontaneous flux density due to superconductivity is evaluated to be $(\Lambda_{0.27\ \mathrm{K}} - \Lambda_{6\ \mathrm{K}}) / (2\pi\gamma_\mu) = 7\ \mu\mathrm{T}$. This maximum value is seven-times smaller than that observed in Sr_2RuO_4 (50 μT) [107]. Thus, we conclude that the time-reversal symmetry is very likely to be preserved in the superconducting state of $Sr_{3-x}SnO$. The preserved time-reversal symmetry is consistent with the theoretically proposed topological phase as well as the ordinary s-wave superconductivity.

6.4 Conclusion of this chapter

We report the first μSR results on the antiperovskite oxide superconductor $Sr_{3-x}SnO$. We successfully observed the superconducting transition in terms of the muon relaxation rate, confirming that the superconductivity originates from the bulk. The temperature dependence of the muon spin depolarization rate, measured in the vortex state of $Sr_{3-x}SnO$ at low temperatures, suggests a fully

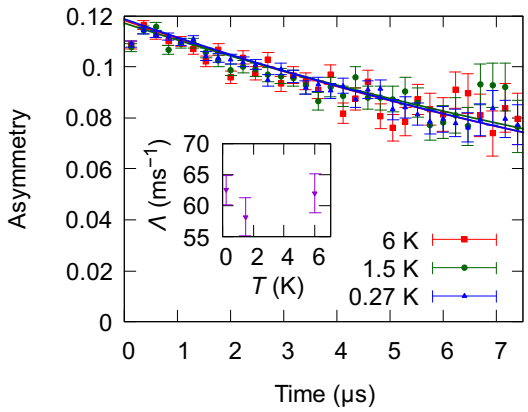

Fig. 6.9 Zero-field μSR spectra of Sample C, recorded at 6 K (red squares), 1.5 K (green circles), and 0.27 K (blue triangles). The solid curves represent the fitting results with the exponential function. Since the signals at different temperatures are on top of each other within the error bars, the time-reversal symmetry is preserved in the superconducting state of $Sr_{3-x}SnO$. Indeed, the temperature dependence of the relaxation rate Λ is quite weak as shown in the inset.

gapped superconductivity. The London penetration depth is estimated to be around 320–1020 nm depending on analyses and samples, and the ratio $T_c/\lambda(0)^{-2}$ is similar to those of high-temperature superconductors or unusual low-carrier superconductors. This fact may hint towards unconventional superconducting mechanism in $Sr_{3-x}SnO$. In addition, we did not detect any sign of the broken time-reversal symmetry. These features do not contradict either with the theoretically proposed topological phase, namely superconductivity similar to the B phase of ^{3}He, or with the conventional s-wave superconductivity.

Chapter 7

Discovery of superconductivity in $CaSb_2$

In this chapter, we report discovery of superconductivity in the nonsymmorphic metal $CaSb_2$ with the transition temperature $T_c = 1.7$ K. We present evidence of bulk superconductivity obtained by means of magnetic susceptibility, resistivity and specific heat. The zero-temperature upper critical field is found to be around 0.2 T, corresponding to the coherence length of 40 nm. We also discuss the possibility of topological superconductivity. The contents in this chapter is based on Ref. [4].

7.1 Evidence of superconductivity

First, we present the PXRD pattern in Fig. 7.1. The pattern revealed that our $CaSb_2$ sample is single phased, except for a slight Al_2O_3 impurity attributable to contamination from the crucible. The lattice parameters of the $CaSb_2$ phase were extracted to be $a = 0.4741$ nm, $b = 0.4182$ nm, $c = 0.9073$ nm, and $\beta = 106.3°$ by the Rietveld analysis with a weighted pattern R value $R_{wp} = 12.7\%$ and goodness of fit $S = 1.21$. The fitting errors were about 0.002%. These lattice parameters are consistent with the previous reports within 0.06% [10, 108].

Next, we show the DC magnetic susceptibility in Fig. 7.2. Strong diamagnetism indicates superconductivity below 1.8 K. The shielding fraction at 0.5 K reaches 77% under 0.5 mT. Assuming the spherical sample shape, the superconducting volume fraction after demagnetization correction is estimated to be 51%. The shielding fraction is suppressed to 16% under 5 mT, suggesting a lower critical field H_{c1} smaller than 5 mT.

Figure 7.3 shows the AC susceptibility of $CaSb_2$. Diamagnetism in the real part of the susceptibility, as well as a small peak in the imaginary part, was observed

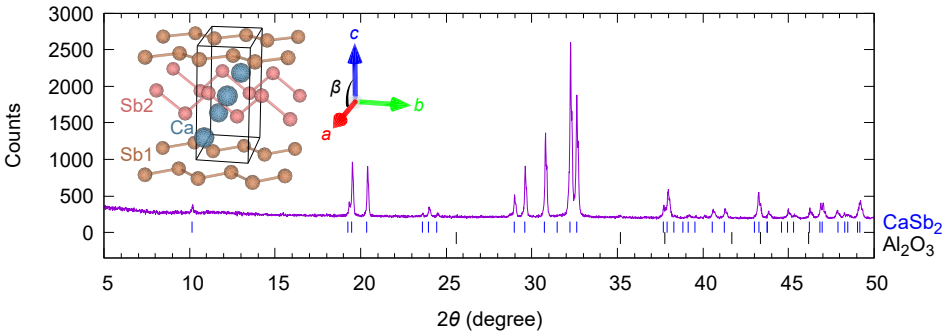

Fig. 7.1 Powder X-ray diffraction pattern of a $CaSb_2$ sample. The lattice parameters of $CaSb_2$ were extracted to be $a = 0.4741$ nm, $b = 0.4182$ nm, $c = 0.9073$ nm, and $\beta = 106.3°$, in agreement with the previous studies [10, 108]. The bars at the bottom indicate the reported peak positions of $CaSb_2$ (blue bars; PDF 01-071-0135) and Al_2O_3 (black bars; PDF 01-089-7716). For our sample, very small peaks of the latter are attributable to a contamination from crucibles. The inset shows the crystalline structure of $CaSb_2$ produced using the program VESTA [67].

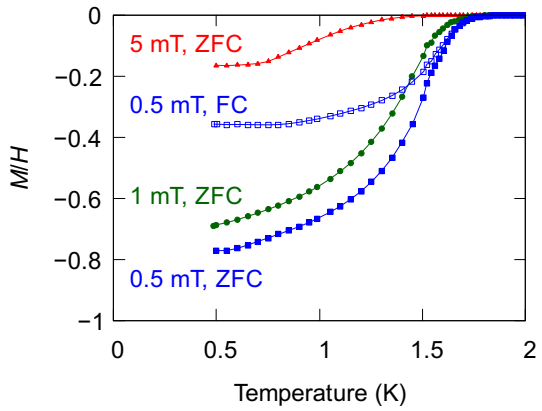

Fig. 7.2 Temperature dependence of the volumetric DC magnetic susceptibility of $CaSb_2$, measured under various fields with zero-field-cooled (ZFC) or field-cooled (FC) conditions. The Meissner effect with the onset of 1.8 K was observed. The shielding fraction reaches 77% at 0.5 K under 0.5 mT with the ZFC process.

with an onset of 1.7 K, with an AC field of 3.3 or 8.2 μT. In addition to the transition at 1.7 K, we observed another broad feature at around 1 K signaled by an additional increase in the diamagnetic signal and by a large and broad peak in the imaginary part. For the following three reasons, we consider that this second feature reflects the percolation of the superconducting current among the polycrystalline grains. Firstly, the shielding fraction changes with the amplitude of the AC field only below the second anomaly as shown in Fig. 7.3. Secondly, the second feature is absent in the DC magnetic susceptibility as shown in Fig. 7.2. Thirdly, the peak of the imaginary part of the AC susceptibility is about 40 times larger at 1 K than at 1.6 K under 3.3 μT, even though the diamagnetism seen in the real part is comparable. These behaviors cannot be explained by the bulk effect and are consistent with the Josephson coupling across the grain boundary. The shielding fraction decreases with increasing AC field because the induced supercurrent exceeds the critical current of the grain boundary. In addition, there is a large energy dissipation due to rapid movement of vortices along the boundary. Similar grain-boundary effect has been reported in various polycrystalline or inhomogeneous materials [109, 110].

The temperature dependence of the resistivity is presented in Fig. 7.4(a). Under cooling at zero field, the resistivity starts to decrease at 1.8 K and reaches zero at 1.2 K. The large resistivity value of 9 mΩ cm in the normal state is probably dominated by scatterings at the grain boundaries. The superconductivity is suppressed as we apply the magnetic field, and above 120 mT the zero resistivity was not observed down to 0.16 K. Figure 7.4(b) shows the superconducting phase diagram deduced from the field dependence of the resistivity. The transition temperature at each field was defined as the temperature at which the resistivity becomes 5, 50, and 95% of the normal-state value. As we can see especially in T_c determined by the 95% criteria, the slope of the phase boundary becomes steeper above 40 mT. This behavior might be related to the second feature observed in the AC susceptibility (Fig. 7.3). Small applied magnetic field may break the superconductivity at the grain boundary. As a result, the resistance increases and consequently the transition temperature rapidly decreases with small field. At relatively low temperature, or in the high-field region in the phase diagram, superconductivity at the grain boundary seems less sensitive to magnetic field. Due to this enhancement, we adopted a linear extrapolation of the upper critical field at the low temperatures instead of the ordinary Werthamer-Helfand-Hohenberg relation. Then the upper critical field at 0 K is estimated to be 0.17–0.26 T depending on the definition of T_c. These values correspond to the Ginzburg-Landau coherence length of $\xi_{GL} = \sqrt{\Phi_0/(2\pi\mu_0 H_{c2})} = 36$–$44$ nm. Using the information of $\mu_0 H_{c1} < 5$ mT, the penetration depth λ and the Ginzburg-Landau parameter $\kappa = \lambda/\xi_{GL}$ are evaluated to be $\lambda > 240$ nm and $\kappa > 5.4$ by solving the equation

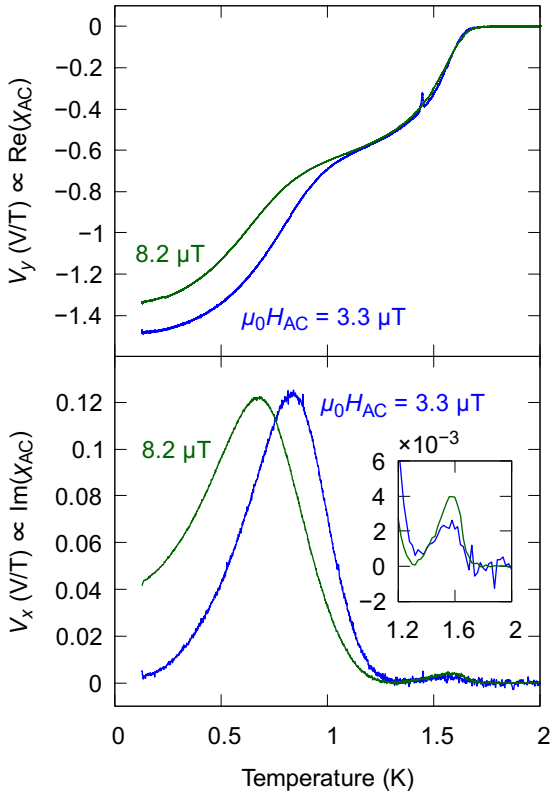

Fig. 7.3 Temperature dependence of voltage signals detected by the mutual inductance coil normalized by the AC-field amplitude. The out-of phase signal V_y and the in-phase signal V_x are proportional to the real and imaginary parts of the AC susceptibility of $CaSb_2$, respectively. These data were obtained under the AC fields with a frequency of 3011 Hz and amplitudes of 3.3 and 8.2 μT. The Meissner effect was observed below 1.7 K. As seen in the inset of the bottom panel, a small peak in the imaginary part was observed. The feature at around 1 K originates from percolation of the superconducting current between the grains (see text).

$\mu_0 H_{c1} = (\ln \kappa)\Phi_0/(4\pi\lambda^2)$ [83].

Finally, we show the temperature dependence of the electronic specific heat $C_e(T)$ in Fig. 7.5(a). We observed a broad but pronounced anomaly starting at 1.5 K. We fitted the data assuming that T_c has a spacial distribution described

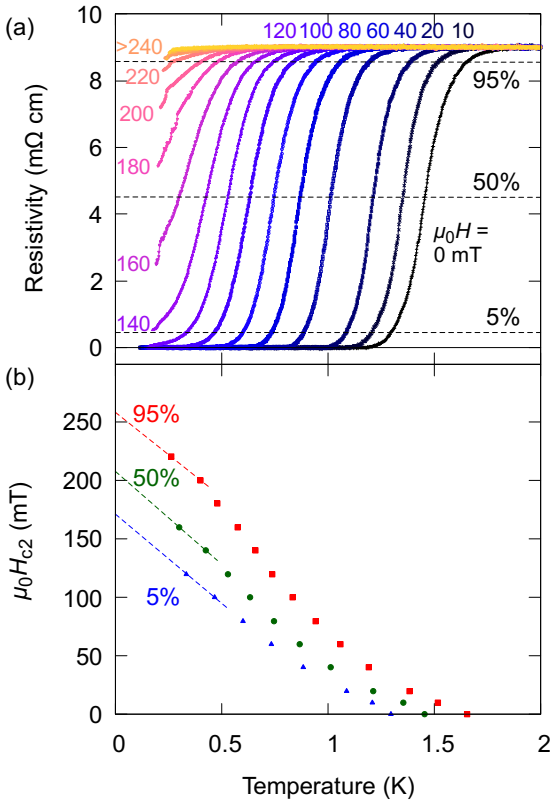

Fig. 7.4 (a) Temperature dependence of the resistivity of $CaSb_2$ measured under 0 mT, 10 mT, and 20 to 280 mT with an interval of 20 mT. Zero resistance was observed below 1.2 K under zero field. The dashed horizontal lines present 5, 50, and 95% of the normal-state value. (b) Superconducting phase diagram deduced from the resistivity data. The transition temperature under each field was defined as the temperature at which the resistivity becomes 5, 50, and 95% of that in the normal state. The dashed lines present the result of the linear fitting to the transition temperatures of each definition. The upper critical field at 0 K was estimated to be 0.17–0.26 T.

by the lognormal distribution:

$$C_P(T) = C_e(T) + \beta T^3, \tag{7.1}$$

$$\frac{C_e(T)}{\gamma T} = 1 + \int_0^{T_o} \left[\frac{C_{\mathrm{BCS}}(T;T_c)}{T} - 1 \right] f_{\mathrm{LN}}(T_o - T_c)\mathrm{d}T_c, \tag{7.2}$$

$$f_{\mathrm{LN}}(x) = \frac{1}{\sqrt{2\pi}\sigma x} \exp\left(-\frac{(\ln x - \mu)^2}{2\sigma^2} \right), \tag{7.3}$$

where $C_P(T)$ is the specific heat including the phononic contribution βT^3 and

$C_{\rm BCS}(T;T_{\rm c})$ is the theoretical specific heat derived from the Bardeen-Cooper-Schrieffer (BCS) theory with a critical temperature of $T_{\rm c}$ [83]. From the fitting, we obtained the Sommerfeld coefficient $\gamma = 2.109(5)$ mJ mol^{-1}K^{-2}, the phononic specific-heat coefficient $\beta = 0.528(3)$ mJ mol^{-1}K^{-4}, and the onset temperature $T_{\rm o} = 1.491(7)$ K. From γ and β, we evaluated the electronic density of states per spin at the Fermi energy $D(E_{\rm F}) = 0.4474(11)$ eV^{-1} per formula unit and the Debye temperature $\Theta_{\rm D} = 222.6(4)$ K. Figure 7.5(b) presents the temperature dependence of the resultant volume-fraction density $f_{\rm LN}(T_{\rm o} - T)$. This probability distribution, restricted to $0 \leq T \leq T_{\rm o}$, has a mode of $T_{\rm mode} = 1.44$ K and median of $T_{\rm med} = 1.08$ K. We can see that $T_{\rm med}$ corresponds to the temperature at which C_e/T is maximum. The superconducting volume fraction at 0.5 K of $\int_{0.5\ {\rm K}}^{T_{\rm o}} f_{\rm LN}(T_{\rm o} - T_{\rm c}){\rm d}T_{\rm c} = 48\%$ is consistent with the value estimated from the magnetic susceptibility within an error of 7%. The volume fraction at 0 K was estimated to be $\int_{0\ {\rm K}}^{T_{\rm o}} f_{\rm LN}(T_{\rm o} - T_{\rm c}){\rm d}T_{\rm c} = 57\%$. This evidences the bulk superconductivity in $CaSb_2$.

We comment that we observed an increase of the specific heat at low temperature under high field (not shown), attributable to the Schottky specific heat from the quadrupole splitting of the Sb nucleus or from the Zeeman splitting of the electronic spin of possible impurities. This contribution is not subtracted from the data taken under zero field. Thus, the volume fraction may be underestimated.

7.2 Discussion

The first-principles calculation shows that $CaSb_2$ hosts two Fermi surfaces near the zone center and the zone boundary with almost the same carrier density [10]. Interestingly, the Fermi surface near the zone boundary encloses high symmetric points A and Z with respect to $P2_1/m$ space group, at which the band forms a four-fold degenerate quartet. The four-fold degeneracy originates from the nonsymmorphic nature of the space group, since it forces an additional orbital degeneracy as well as Kramers spin degeneracy [10]. Moreover, a cylindrical Fermi surface along the AZ line (parallel to the c axis) originates from a slightly electron-doped band with a four-fold line-nodal degeneracy near its bottom. Because of this band structure, the Fermi surface exhibits a large orbit and spin mixing. Therefore, in a similar manner to doped topological insulators [17] and doped Dirac semimetals [8, 28], topological superconductivity is naturally expected if the inter-orbital pairing interaction is dominant. In fact,the zig-zag chain consisting of two Sb1 sites in the unit cell may host such inter-orbital Cooper pairing. Another interesting possibility is a time-reversal-breaking chiral p-wave superconductivity [37]. Whereas the present system has a cylindrical Fermi surface not a torus one discussed in Ref. [37], and the relevant space group symmetry is different, it has the same fea-

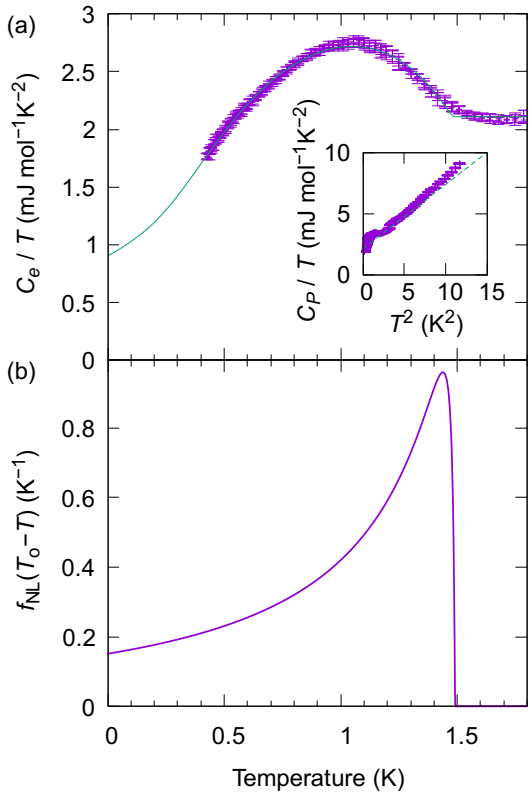

Fig. 7.5 (a) Temperature dependence of the electronic specific heat divided by temperature, evidencing the bulk superconductivity. The solid curve presents the fitting with the BCS theory with a spatial distribution of the critical temperature. The volume fraction is estimated to be 57%. The inset shows the total specific heat including the phononic contribution divided by temperature plotted against T^2. The dashed line indicates the normal-state specific heat $C_P/T = \gamma + \beta T^2$. (b) The volume-fraction density $f_{\mathrm{LN}}(T_\mathrm{o} - T)$ as a function of temperature. Starting from $T_\mathrm{o} = 1.49$ K, the largest population exhibits superconductivity at $T_\mathrm{mode} = 1.44$ K and half of the superconductive part becomes superconducting at $T_\mathrm{med} = 1.08$ K.

ture that the Fermi surface originates from a nodal line. Therefore, the mechanism for chiral p-wave superconductivity in Ref. [37] might work as well.

7.3 Conclusion of this chapter

We report the discovery of superconductivity in $CaSb_2$, which has nodal lines in the bulk electronic band structure crossing the Fermi energy, protected by a

nonsymmorphic crystalline symmetry. Both DC magnetization and specific heat indicate the bulk superconductivity. The transition temperature is determined to be 1.7 K from magnetic susceptibility and resistivity. The lower critical field is smaller than 5 mT, and the upper critical field is estimated to be 0.17–0.26 T. From these critical fields, the Ginzburg-Landau parameter is evaluated to be $\kappa > 5.4$.

Chapter 8

Conclusion

8.1 Summary

We measured high-energy XRD for superconductive $Sr_{3-x}SnO$ and observed no evidence of the superstructure caused by Sr deficiency. Then, we calculated the band structure of $Sr_{2.5}SnO$ using a supercell method and coherent potential approximation. Both calculations suggest heavy hole doping of about 0.8 eV due to Sr deficiency. Since the topological superconductivity is suppressed with heavy doping, Sr deficiency of $x = 0.01$ will be favorable to the topological superconductivity.

We reported the temperature dependence of the ^{119}Sn-M"ossbauer spectra of $Sr_{3-x}SnO$ down to 3 K. As a result, we observed the metallic anion Sn^{4-} and additional ionic state of Sn. From the comparison to the first-principles calculations in terms of the isomer shift and the Debye temperature, we identified the additional state to be the Sn atoms with neighboring Sr deficiency and deduced the local composition to be around "$Sr_3Sn_2O_2$." This result confirms the hole doping to Sn as calculations suggested.

For the superconducting state, we carried out μSR experiments and evaluated the London penetration depth λ. The estimated penetration depth is long for a superconductor with $T_c = 5$ K, with the ratio $T_c/\lambda(0)$ comparable to high-temperature or low-carrier superconductors. This possibly hint towards unconventional pairing mechanism in $Sr_{3-x}SnO$. The temperature dependence of λ indicate that a fully gapped state is more likely than a nodal state.

In addition to the various properties of $Sr_{3-x}SnO$, we reported a discovery of superconductivity in $CaSb_2$ with $T_c = 1.7$ K and $H_{c2} \simeq 0.2$ T, evidenced by the Meissner effect and zero resistance. The volume fraction is estimated to be around 50% from the magnetic-susceptibility and specific-heat measurements.

We expect that the microscopic understanding of the novel ionic states will lead to new chemistry and physics of metallic anions and will also contribute to

development of the Mössbauer spectroscopy. We also hope that these results on $Sr_{3-x}SnO$ and $CaSb_2$ will be useful for the research of general Dirac and line-nodal superconductors, as well as for determination of the superconducting-gap symmetry in $Sr_{3-x}SnO$.

8.2 Future perspective

Our Mössbauer study revealed that there is spontaneous Sr deficiency even in the nearly stoichiometric $Sr_{3-x}SnO$. Thus, compensation of the spontaneous doping for example by substitution of Sn to Sb will be interesting. With the Fermi energy exactly at the Dirac point, peculiar properties will be clearer in NMR and other techniques. It is also interesting to search for superconductivity in the electron-doped region. For the deficient sample, measurement of the Sr-Sr distance by the extended x-ray absorption fine structure (EXAFS) or by the pair-distribution function (PDF) will give us important information.

To detect the line-nodal property of $CaSb_2$, ARPES will be favorable because in any transport measurements, the properties of the nodal line will be masked by the conventional bands. Anisotropy measurements of the superconducting gap will make it clear whether the superconductivity is topological or not. Thus, single-crystal growth should be tried. Since this is a binary compound and the phase diagram is available, flux method is likely to be successful.

Acknowledgements

I thank Prof. Y. Maeno for his supervision for more than five years, including direction of this project, long and frequent discussions, connecting people for collaborations, and improving my presentation skills. I also thank Associate Prof. S. Yonezawa for innumerable assistance in all aspects of research i.e. experiment, theory, gnuplot, LaTeX, computing, etc.

I'm grateful to all the collaborators. I thank Associate Prof. S. Kitao and Prof. M. Seto regarding Mössbauer spectroscopy. I thank Prof. M. Sato, Assistant Prof. S. Kobayashi, Assistant Prof. T. Kawakami, and Dr. T. Hashimoto for theoretical analyses. I especially acknowledge Mr. T. Fukumoto for teaching me first-principles calculation and Prof. Y. Tanaka and Assistant Prof. K. Yada for accepting my visit to Nagoya University. I also thank Dr. H. Takatsu, Associate Prof. C. Tassel, Dr. F. Takeiri, and Prof. H. Kageyama for the opportunity of high-energy XRD. I appreciate the technical support and discussions regarding μSR from Dr. Z. Guguchia, Dr. Das, Mr. Baines, Dr. Shiroka, and Dr. Luetkens.

My research has been helped by lots of kindness. I thank Dr. T. Watashige, Assistant Prof. S. Kasahara, Associate Prof. Y. Kasahara, and Prof. Y. Matsuda for sharing equipments and techniques. I thank Prof. I. R. Fisher, Mr. E. Rosenberg, Mr. J. Straquadine, and Ms. J. Palmstrom for accepting my visit to Stanford University and teaching me crystal growth. I also thank Associate Prof. A. Otsuka for letting me use the hydraulic press and Associate Prof. M. Maesato for letting me use the glovebox. I acknowledge ORION CYCLE for providing us with the puncture-repair kit. I thank Assistant Prof. H. Gomi and Computational Materials Design Workshop for the instruction in AkaiKKR (Machikaneyama).

Many discussions improved my work. I thank Prof. M. Sigrist and Dr. J. Lado for accepting my visit to ETH Zürich and giving me the opportunity to talk with many people. I also thank Assistant Prof. Y. Kobayashi and Dr. R. Masuda for various supports at the Institute for Integrated Radiation and Nuclear Science. I thank Prof. Y. J. Uemura for initiating the μSR project and providing useful suggestions. I appreciate discussions with Dr. V. Grinenko and Dr. W. Higemoto regarding μSR.

I'm grateful to members of and visitors to the Quantum Materials Laboratory. I thank Prof. K. Ishida and Assistant Prof. S. Kitagawa for all the guidance,

discussions, and enjoyable time. I particularly acknowledge Associate Prof. M. Polo J. S. for guidance at the very first stage of my research life. I appreciate all the endeavor in this project by Dr. M. Oudah, Mr. J. N. Hausmann, Mr. S. Koibuchi, Mr. H. G. Lee, Mr. I. Marković, and Mr. M. Kawaguchi. I also thank the other group members for enjoyable time in the laboratory. Especially Mr. K. Tajiri and Mr. H. Suwa added a bit of spice in my research life. I appreciate all the administrative work by Ms. K. Takamiya and Ms. Y. Ito and web management by Ms. T. Kodama.

I acknowledge the JSPS Research Fellowship by Japan Society for Promotion of Science (JSPS).

Bibliography

[1] A. Ikeda, T. Fukumoto, M. Oudah, J. N. Hausmann, S. Yonezawa, S. Kobayashi, M. Sato, C. Tassel, F. Takeiri, H. Takatsu, H. Kageyama, and Y. Maeno, Physica B Condens. Matter **536**, 752 (2018).

[2] A. Ikeda, S. Koibuchi, S. Kitao, M. Oudah, S. Yonezawa, M. Seto, and Y. Maeno, Phys. Rev. B **100**, 245145 (2019).

[3] A. Ikeda, Z. Guguchia, M. Oudah, S. Koibuchi, S. Yonezawa, D. Das, T. Shiroka, H. Luetkens, and Y. Maeno, submitted to Phys. Rev. B.

[4] A. Ikeda, M. Kawaguchi, S. Koibuchi, T. Hashimoto, T. Kawakami, S. Yonezawa, M. Sato, and Y. Maeno, submitted to Phys. Rev. Mater.

[5] T. Kariyado and M. Ogata, J. Phys. Soc. Jpn. **80**, 083704 (2011).

[6] T. H. Hsieh, J. Liu, and L. Fu, Phys. Rev. B **90**, 081112(R) (2014).

[7] M. Oudah, A. Ikeda, J. N. Hausmann, S. Yonezawa, T. Fukumoto, S. Kobayashi, M. Sato, and Y. Maeno, Nat. Commun. **7**, 13617 (2016).

[8] T. Kawakami, T. Okamura, S. Kobayashi, and M. Sato, Phys. Rev. X **8**, 041026 (2018).

[9] M. Oudah, J. N. Hausmann, S. Kitao, A. Ikeda, S. Yonezawa, M. Seto, and Y. Maeno, Sci. Rep. **9**, 1831 (2019).

[10] K. Funada, A. Yamakage, N. Yamashina, and H. Kageyama, J. Phys. Soc. Jpn. **88**, 044711 (2019).

[11] M. Z. Hasan and C. L. Kane, Rev. Mod. Phys. **82**, 3045 (2010).

[12] X.-L. Qi and S.-C. Zhang, Rev. Mod. Phys. **83**, 1057 (2011).

[13] Y. Ando, J. Phys. Soc. Jpn. **82**, 102001 (2013).

[14] Y. Tanaka, M. Sato, and N. Nagaosa, J. Phys. Soc. Jpn. **81**, 011013 (2012).

[15] M. Sato and S. Fujimoto, J. Phys. Soc. Jpn. **85**, 072001 (2016).

[16] M. Sato and Y. Ando, Reports on Progress in Physics **80**, 076501 (2017).

[17] L. Fu and E. Berg, Phys. Rev. Lett. **105**, 097001 (2010).

[18] S. Sasaki, M. Kriener, K. Segawa, K. Yada, Y. Tanaka, M. Sato, and Y. Ando, Phys. Rev. Lett. **107**, 217001 (2011).

[19] K. Matano, M. Kriener, K. Segawa, Y. Ando, and G.-q. Zheng, Nat. Phys. **12**, 852 (2016).

[20] S. Yonezawa, K. Tajiri, S. Nakata, Y. Nagai, Z. Wang, K. Segawa, Y. Ando, and Y. Maeno, Nat. Phys. **13**, 123 (2017).

[21] K. Yamada and T. Ohmi: *Superfluidity* (Baifukan, Tokyo, Jul. 1995).
[22] Y. Maeno, S. Kittaka, T. Nomura, S. Yonezawa, and K. Ishida, J. Phys. Soc. Jpn. **81**, 011009 (2012).
[23] A. de Visser and J. Franse, J. Magn. Magn. Mater. **100**, 204 (1991).
[24] L. Aggarwal, A. Gaurav, G. S. Thakur, Z. Haque, A. K. Ganguli, and G. Sheet, Nat. Mater. **15**, 32 (2016).
[25] J. J. Neumeier and M. G. Smith, Physica C **542**, 1 (2017).
[26] B. Yan and C. Felser, Annu. Rev. Condens. Matter. Phys. **8**, 337 (2017).
[27] N. P. Armitage, E. J. Mele, and A. Vishwanath, Rev. Mod. Phys. **90**, 015001 (2018).
[28] S. Kobayashi and M. Sato, Phys. Rev. Lett. **115**, 187001 (2015).
[29] Y. Li and F. D. M. Haldane, Phys. Rev. Lett. **120**, 067003 (2018).
[30] L. He, Y. Jia, S. Zhang, X. Hong, C. Jin, and S. Li, npj Quantum Mater. **1**, 16014 (2016).
[31] C. Fang, Y. Chen, H.-Y. Kee, and L. Fu, Phys. Rev. B **92**, 081201 (2015).
[32] A. Yamakage, Y. Yamakawa, Y. Tanaka, and Y. Okamoto, J. Phys. Soc. Jpn. **85**, 013708 (2016).
[33] S. Kobayashi, Y. Yamakawa, A. Yamakage, T. Inohara, Y. Okamoto, and Y. Tanaka, Phys. Rev. B **95**, 245208 (2017).
[34] Y. Huh, E.-G. Moon, and Y. B. Kim, Phys. Rev. B **93**, 035138 (2016).
[35] M. Hirayama, R. Okugawa, T. Miyake, and S. Murakami, Nat. Commun. **8**, 14022 (2017).
[36] S. T. Ramamurthy and T. L. Hughes, Phys. Rev. B **95**, 075138 (2017).
[37] H. Shapourian, Y. Wang, and S. Ryu, Phys. Rev. B **97**, 094508 (2018).
[38] J. G. Bednorz and K. A. Müller, Z. Phys. B **64**, 189 (1986).
[39] A. P. Drozdov, M. I. Eremets, I. A. Troyan, V. Ksenofontov, and S. I. Shylin, Nature **525**, 73 (2015).
[40] M. Somayazulu, M. Ahart, A. K. Mishra, Z. M. Geballe, M. Baldini, Y. Meng, V. V. Struzhkin, and R. J. Hemley, Phys. Rev. Lett. **122**, 027001 (2019).
[41] A. Widera and H. Schafer, Mater. Res. Bull. **15**, 1805 (1980).
[42] T. Kariyado and M. Ogata, J. Phys. Soc. Jpn. **81**, 064701 (2012).
[43] T. Kariyado and M. Ogata, Phys. Rev. Mater. **1**, 061201 (2017).
[44] J. Nuss, C. Mühle, K. Hayama, V. Abdolazimi, and H. Takagi, Acta Cryst. B **71**, 300 (2015).
[45] Y. Obata, R. Yukawa, K. Horiba, H. Kumigashira, Y. Toda, S. Matsuishi, and H. Hosono, Phys. Rev. B **96**, 155109 (2017).
[46] Y. Obata, Y. Kohama, S. Matsuishi, and H. Hosono, Phys. Rev. B **99**, 115133 (2019).
[47] S. Suetsugu, K. Hayama, A. W. Rost, J. Nuss, C. Mühle, J. Kim, K. Kitagawa, and H. Takagi, Phys. Rev. B **98**, 115203 (2018).

[48] N. Werthamer, E. Helfand, and P. Hohenberg, Phys. Rev. **147**, 295 (1966).
[49] J. N. Hausmann, M. Oudah, A. Ikeda, S. Yonezawa, and Y. Maeno, Supercond. Sci. Technol. **31**, 055012 (2018).
[50] S. Kitagawa, K. Ishida, M. Oudah, J. N. Hausmann, A. Ikeda, S. Yonezawa, and Y. Maeno, Phys. Rev. B **98**, 100503(R) (2018).
[51] M. N. Ali, Q. D. Gibson, T. Klimczuk, and R. J. Cava, Phys. Rev. B **89**, 020505 (2014).
[52] J.-M. Carter, V. V. Shankar, M. A. Zeb, and H.-Y. Kee, Phys. Rev. B **85**, 115105 (2012).
[53] Y. Chen, Y.-M. Lu, and H.-Y. Kee, Nat. Commun. **6**, 6593 (2015).
[54] Q.-F. Liang, J. Zhou, R. Yu, Z. Wang, and H. Weng, Phys. Rev. B **93**, 085427 (2016).
[55] Y. Sun, Y. Zhang, C.-X. Liu, C. Felser, and B. Yan, Phys. Rev. B **95**, 235104 (2017).
[56] H. Okamoto, J. Phase Equilibria **18**, 313 (1997).
[57] S. Yonezawa, T. Higuchi, Y. Sugimoto, C. Sow, and Y. Maeno, Rev. Sci. Instrum. **86**, 093903 (2015).
[58] E. Fujita, S. Nasu, and Y. Yoshida: *Introduction to Mössbauer Spectroscopy: its Principles and Applications* (AGNE Gijutsu Center Inc., Tokyo, Jul. 1999).
[59] J. G. Stevens, Hyperfine Interactions **13**, 221 (1983).
[60] A. A. Bahgat, Phys. Status Solidi A **63**, K39 (1981).
[61] E. H. Brandt, Phys. Rev. B **37**, 2349 (1988).
[62] P. Blaha, K. Schwarz, G. Madsen, D. Kvasnicka, and J. Luitz. *WIEN2k, An Augmented Plane Wave Plus Local Orbital Program for Calculating Crystal Properties*. Vienna University of Technology Institute of Materials Chemistry, Vienna, Austria, Dec 2016.
[63] K. Sato, M. Ogura, and H. Akai. *Band structure calculation using KKR-Green's function method*, Aug 2008.
[64] J. Korringa, Physica **13**, 392 (1947).
[65] W. Kohn and N. Rostoker, Phys. Rev. **94**, 1111 (1954).
[66] J. P. Perdew, K. Burke, and M. Ernzerhof, Phys. Rev. Lett. **77**, 3865 (1996).
[67] K. Momma and F. Izumi, J. Appl. Crystallogr. **44**, 1272 (2011).
[68] A. Kokalj, Computational Materials Science **28**, 155 (2003).
[69] H. Shiba, Progress of Theoretical Physics **46**, 77 (1971).
[70] P. Soven, Phys. Rev. B **2**, 4715 (1970).
[71] J. Batool, S. M. Alay-e Abbas, A. Ali, K. Mahmood, S. Akhtar, and N. Amin, RSC Adv. **7**, 6880 (2017).
[72] L. Fournès, J. Grannec, Y. Potin, and P. Hagenmuller, Solid State Commun. **59**, 833 (1986).
[73] J. Bashir, R. T. A. Khan, N. M. Butt, and G. Heger, Powder Diffraction **17**,

222 (2002).
[74] Y. F. Lee, F. Wu, R. Kumar, F. Hunte, J. Schwartz, and J. Narayan, Appl. Phys. Lett. **103**, 112101 (2013).
[75] Y. F. Lee, J. Narayan, and J. Schwartz, J. Appl. Phys. **116**, 164903 (2014).
[76] P. Z. Hien, V. S. Shpinel', A. S. Viskov, and Y. N. Venevtsev, J. Exp. Theor. Phys. **17**, 1271 (1963).
[77] H. Micklitz and P. H. Barrett, Phys. Rev. B **5**, 1704 (1972).
[78] J. Bolz and F. Pobell, Zeitschrift für Physik B Condensed Matter **20**, 95 (1975).
[79] C. Hohenemser, Phys. Rev. **139**, A185 (1965).
[80] A. Svane, N. E. Christensen, C. O. Rodriguez, and M. Methfessel, Phys. Rev. B **55**, 12572 (1997).
[81] R. Kurian and M. Filatov, J. Chem. Phys. **130**, 124121 (2009).
[82] R. Balian and N. R. Werthamer, Phys. Rev. **131**, 1553 (1963).
[83] M. Tinkham: *Introduction to Superconductivity* (Dover Publications, New York, 2004).
[84] K. Hasselbach, J. R. Kirtley, and J. Flouquet, Phys. Rev. B **47**, 509 (1993).
[85] R. W. Shaw, D. E. Mapother, and D. C. Hopkins, Phys. Rev. **120**, 88 (1960).
[86] Y. J. Uemura, G. M. Luke, B. J. Sternlieb, J. H. Brewer, J. F. Carolan, W. N. Hardy, R. Kadono, J. R. Kempton, R. F. Kiefl, S. R. Kreitzman, P. Mulhern, T. M. Riseman, D. L. Williams, B. X. Yang, S. Uchida, H. Takagi, J. Gopalakrishnan, A. W. Sleight, M. A. Subramanian, C. L. Chien, M. Z. Cieplak, G. Xiao, V. Y. Lee, B. W. Statt, C. E. Stronach, W. J. Kossler, and X. H. Yu, Phys. Rev. Lett. **62**, 2317 (1989).
[87] Y. J. Uemura, L. P. Le, G. M. Luke, B. J. Sternlieb, W. D. Wu, J. H. Brewer, T. M. Riseman, C. L. Seaman, M. B. Maple, M. Ishikawa, D. G. Hinks, J. D. Jorgensen, G. Saito, and H. Yamochi, Phys. Rev. Lett. **66**, 2665 (1991).
[88] C. Kittel: *Introduction to Solid State Physics* (Wiley, New York, 2005).
[89] C. Collignon, B. Fauqué, A. Cavanna, U. Gennser, D. Mailly, and K. Behnia, Phys. Rev. B **96**, 224506 (2017).
[90] T. Bay, M. Jackson, C. Paulsen, C. Baines, A. Amato, T. Orvis, M. Aronson, Y. Huang, and A. de Visser, Solid State Commun. **183**, 13 (2014).
[91] J. A. Krieger, A. Kanigel, A. Ribak, E. Pomjakushina, K. B. Chashka, K. Conder, E. Morenzoni, T. Prokscha, A. Suter, and Z. Salman, JPS Conf. Proc. **21**, 011028 (2018).
[92] J. Kim, F. Ronning, N. Haberkorn, L. Civale, E. Nazaretski, N. Ni, R. J. Cava, J. D. Thompson, and R. Movshovich, Phys. Rev. B **85**, 180504 (2012).
[93] R. Khasanov, H. Luetkens, A. Amato, H.-H. Klauss, Z.-A. Ren, J. Yang, W. Lu, and Z.-X. Zhao, Phys. Rev. B **78**, 092506 (2008).
[94] H. Luetkens, H.-H. Klauss, M. Kraken, F. J. Litterst, T. Dellmann, R. Klingeler, C. Hess, R. Khasanov, A. Amato, C. Baines, M. Kosmala, O. J.

Schumann, M. Braden, J. Hamann-Borrero, N. Leps, A. Kondrat, G. Behr, J. Werner, and B. Buchner, Nat. Mater. **8**, 305 (2009).
[95] F. L. Pratt, P. J. Baker, S. J. Blundell, T. Lancaster, H. J. Lewtas, P. Adamson, M. J. Pitcher, D. R. Parker, and S. J. Clarke, Phys. Rev. B **79**, 052508 (2009).
[96] Z. Shermadini, J. Kanter, C. Baines, M. Bendele, Z. Bukowski, R. Khasanov, H.-H. Klauss, H. Luetkens, H. Maeter, G. Pascua, B. Batlogg, and A. Amato, Phys. Rev. B **82**, 144527 (2010).
[97] Z. Guguchia, Z. Shermadini, A. Amato, A. Maisuradze, A. Shengelaya, Z. Bukowski, H. Luetkens, R. Khasanov, J. Karpinski, and H. Keller, Phys. Rev. B **84**, 094513 (2011).
[98] T. M. Riseman, P. G. Kealey, E. M. Forgan, A. P. Mackenzie, L. M. Galvin, A. W. Tyler, S. L. Lee, C. Ager, D. M. Paul, C. M. Aegerter, R. Cubitt, Z. Q. Mao, T. Akima, and Y. Maeno, Nature **396**, 242 (1998).
[99] L. P. Le, G. M. Luke, B. J. Sternlieb, W. D. Wu, Y. J. Uemura, J. W. Brill, and H. Drulis, Physica C: Superconductivity **185–189**, 2715 (1991).
[100] Z. Guguchia, F. von Rohr, Z. Shermadini, A. T. Lee, S. Banerjee, A. R. Wieteska, C. A. Marianetti, B. A. Frandsen, H. Luetkens, Z. Gong, S. C. Cheung, C. Baines, A. Shengelaya, G. Taniashvili, A. N. Pasupathy, E. Morenzoni, S. J. L. Billinge, A. Amato, R. J. Cava, R. Khasanov, and Y. J. Uemura, Nat. Commun. **8**, 1082 (2017).
[101] F. O. von Rohr, J.-C. Orain, R. Khasanov, C. Witteveen, Z. Shermadini, A. Nikitin, J. Chang, A. R. Wieteska, A. N. Pasupathy, M. Z. Hasan, A. Amato, H. Luetkens, Y. J. Uemura, and Z. Guguchia, Sci. Adv. **5** (2019).
[102] Y. J. Uemura, A. Keren, L. P. Le, G. M. Luke, B. J. Sternlieb, W. D. Wu, J. H. Brewer, R. L. Whetten, S. M. Huang, S. Lin, R. B. Kaner, F. Diederich, S. Donovan, G. Gruner, and K. Holczer, Nature **352**, 605 (1991).
[103] A. Gauzzi, J. Le Cochec, G. Lamura, B. J. Jönsson, V. A. Gasparov, F. R. Ladan, B. Plaçais, P. A. Probst, D. Pavuna, and J. Bok, Rev. Sci. Instrum. **71**, 2147 (2000).
[104] X. H. Chen, Y. Y. Xue, R. L. Meng, and C. W. Chu, Phys. Rev. B **64**, 172501 (2001).
[105] A. Carrington and F. Manzano, Physica C Supercond. **385**, 205 (2003).
[106] A. Shengelaya, R. Khasanov, D. G. Eshchenko, D. Di Castro, I. M. Savić, M. S. Park, K. H. Kim, S.-I. Lee, K. A. Müller, and H. Keller, Phys. Rev. Lett. **94**, 127001 (2005).
[107] G. M. Luke, Y. Fudamoto, K. M. Kojima, M. I. Larkin, J. Merrin, B. Nachumi, Y. J. Uemura, Y. Maeno, Z. Q. Mao, Y. Mori, H. Nakamura, and M. Sigrist, Nature **394**, 558 (1998).
[108] K. Deller and B. Eisenmann, Z. Anorg. Allg. Chem. **425**, 104 (1976).
[109] M. Yang, Y. H. Kao, Y. Xin, and K. W. Wong, Phys. Rev. B **50**, 13653

(1994).
[110] S. Kittaka, T. Nakamura, H. Yaguchi, S. Yonezawa, and Y. Maeno, J. Phys. Soc. Jpn. **78**, 064703 (2009).